# Selective vulnerability of cerebral vasculature to *NOTCH3* variants in small vessel disease and rescue by phosphodiesterase-5 inhibitor

Xiangjun Zhao[1], Chaowen Yu[1,2], Antony Adamson[3], Aite Zhao[4], Huiyu Zhou[5], Pankaj Sharma[6] & Tao Wang[1,7,8]*

[1]Devision of Evolution, Infection and Genomic Sciences, School of Biological Sciences, Faculty of Biology, Medicine, and Health, The University of Manchester, UK
[2]Children's Hospital of Chongqing Medical University, Chongqing, 400014, P.R. China
[3]Genome Editing Unit, Faculty of Biology, Medicine and Health, The University of Manchester, UK
[4]College of Computer Science and Technology, Qingdao University, P.R. China
[5]School of Computing and Mathematical Sciences, University of Leicester, UK
[6]Institute of Cardiovascular Research, Royal Holloway, University of London, Ashford and St Peter's NHS Foundation Trust, and Imperial College Healthcare NHS Trust, London, UK
[7]Manchester Centre for Genomic Medicine, Manchester University NHS Foundation Trust, Manchester, UK
[8]Geoffrey Jefferson Brain Research Centre, Manchester Academic Health Science Centre, Northern Care Alliance & University of Manchester, Manchester, UK

* Corresponding Author: tao.wang@manchester.ac.uk

## Abstract

*NOTCH3* variants cause CADASIL the most common genetic form of small vessel disease (SVD) and vascular dementia (VaD) and increase the stroke and SVD/VaD risk. CADASIL is a systemic vasculopathy but predominantly manifests in the brain. The molecular mechanisms of CADASIL remain largely unclear with no specific available treatments. *NOTCH3* is primarily expressed in vascular smooth muscle cells (VSMCs). Using human induced pluripotent stem cell (iPSC) models and developmental lineage-specific VSMC differentiation, we revealed a selective vulnerability of cerebral but not peripheral VSMC mimics to *NOTCH3* variants. Transcriptomic, protein and functional analyses demonstrated a switching of CADASIL iPSC-VSMCs from a contractile to a synthetic phenotype, accompanied with extensive extracellular matrix accumulation and impairment of cell adhesion leading to *anoikis*. Importantly, we describe an endothelial independent nitric oxide signalling in VSMCs which was dysregulated in the CADASIL iPSC-VSMCs, and posphodiesterase-5 (PDE5) inhibition successfully rescued the abnormal VSMC function, suggesting a novel therapeutic strategy. Our findings offer new mechanistic insights into brain specific phenotype in *NOTCH3*-associated SVD/VaD and support patient-specific iPSCs to be a valuable model for identifying targeted treatment for *NOTCH3*-associated SVD/VaD.

**Keywords**: CADASIL, genetic small vessel disease, vascular dementia, *NOTCH3*, VSMC phenotype, extracellular matrix, nitric oxide signalling, PDE5 inhibitor

## Introduction

Small vessel disease (SVD) is the leading cause of vascular dementia (VaD) and the second commonest cause of dementia after Alzheimer's disease[1]. Genetic factors play an important role in the susceptibility, development and progression of SVD[2,3]. *NOTCH3* variants cause CADASIL (cerebral autosomal dominant arteriopathy and subcortical infarcts and leukoencephalopathy), the most common form of genetic SVD[4,5]. This rare genetic form of SVD has an estimated prevalence of 2-4 per 100,000 individuals, but CADASIL-like *NOTCH3* variants are more common than expected with an overall frequency of ~1:300 in the general population and associated with a significantly increased risk of sporadic stroke and SVD/VaD[6-8]. CADASIL is a systemic vasculopathy affecting small vessels throughout the body, but its clinical manifestations are mainly in the brain. Patients with CADASIL typically experience recurrent strokes, and many also suffer from migraine with aura and mood disturbance gradually progressing to cognitive impairment and eventually, vascular dementia (VaD)[9-11]. The exact molecular mechanisms by which *NOTCH3* variants lead to neurological symptoms remain unclear; and consequently, no specific or effective treatments are currently available.

*NOTCH3* is one of the four Notch receptors transducing Notch signalling predominantly expressed in arterial vascular smooth muscle cells (VSMCs), where it promotes differentiation and proliferation, prevents migration, and protects VSMCs against apoptosis[12-16], playing a key role in maintaining vascular homeostasis. Unlike Notch1 or Notch2, depletion of which is embryonically lethal, *Notch3* knockout mice are viable but display abnormal VSMC maturation and venous characteristics[13]. In CADASIL, the hallmark pathological changes are VSMC degeneration, Notch3 protein accumulation, and granular osmophilic material (GOM)

deposition in small arteries[10,16-18]. However, *NOTCH3* knockout mice do not have typical CADASIL phenotype[13] , and RBP-Jκ mediated canonical Notch signalling remains active in transgenic CADASIL mice[19], suggesting the disease is not due to a simple loss of function. Instead, toxic gain-of-function from protein aggregation likely drives disease progression[9]. Given that Notch signalling cross-talks with multiple signalling pathways, including the Wnt[20,21], hedgehog (Hg)[22], transforming growth factor-beta (TGF-β)[23], PI3K/Akt[21,24], MAPK/ERK[25], and nitric oxide (NO)[26] signalling pathways, it remains unclear whether and in what way mutant *NOTCH3* disrupts the crosstalk and contributes to the development of CADASIL pathology. Understanding this mechanism could have important therapeutic implications.

VSMCs are developmentally heterogeneous[27,28]. Neural crest cells form VSMCs in the ascending aorta and cerebral vessels; lateral plate mesoderm contributes to VSMCs in the aortic root and coronary arteries via epicardium; paraxial mesoderm generates VSMCs in peripheral vessels. Lineage-specific VSMCs have differential responses to growth factors like angiotensin II[29] and TGF-β[30], and show varying disease susceptibilities, independent of hemodynamic factors; for instance, Marfan's syndrome affects the aorta root and ascending aorta[31,32], while atherosclerotic targets the aortic arch[33,34]. *NOTCH3* is systemically expressed throughout in vasculature, its lineage-specific susceptibility to *NOTCH3* variants remain unexplored, leaving a key knowledge gap in understanding the brain-predominant clinical features in CADASIL.

VSMCs are not terminally differentiated cells and exhibit phenotypic plasticity in response to different stimuli[35,36]. In healthy arteries they exhibit a contractile phenotype, but under pathological conditions like atherosclerosis, vascular injury or restenosis, they undergo dedifferentiation and acquire a synthetic phenotype by downregulating contractile markers and increasing production of extracellular matrix (ECM) proteins, growth factors and cytokines, leading to proliferation and migration[27,28]. In CADASIL, VSMC phenotype switching has not been systemically studied, despite impaired vasoreactivity observed in both patients and transgenic mice[37-39]. A deeper understanding of VSMC plasticity in CADASIL is crucial to uncover disease mechanisms and informing therapeutic strategies.

To date, over a dozen CADASIL mouse models have been developed, which uncovered valuable insights into molecular mechanisms of the disease. While the models successfully phenocopy key pathological features of CADASIL, such as VSMC degeneration, GOM deposition and Notch3 accumulation, most failed to recapitulate the full range of neurological symptoms observed in human patients[40]. Given that 90% of drugs that pass preclinical testing in animal models ultimately fail to reach patients[41], there is a critical need for human disease models as complimentary tools for studying disease mechanisms and advancing drug development. In this regard, induced pluripotent stem cells (iPSCs) derived from CADASIL patients provide a powerful platform for better understanding of this condition and accelerating therapeutic discovery.

We previously established iPSC models of CADASIL from patient skin biopsies, revealing that CADASIL VSMCs failed to stabilise angiogenic capillary structures and support blood-brain barrier (BBB) integrity[42,43]. In this study, we generated developmental lineage-specific VSMCs and identified a selective vulnerability of neural crest derived VSMCs to *NOTCH3* variants, which likely explain the brain-specific manifestation in CADASIL. Results provide convincing evidence of VSMC phenotype switching and demonstrate accumulations of ECM proteins and impaired VSMC adhesion leading to *anoikis* type of cell death. The local NO signalling in CADASIL was impaired with reduced soluble guanylyl cyclase (sGC) in the CADASIL iPSC-

VSMCs. Treatment with an NO donor or phosphodiesterase type 5 (PDE5) inhibitor (sildenafil) significantly reversed VSMC dysfunction and cell death, suggesting a promising therapeutic approach for CADASIL.

## Results

### IPSC-derived brain-specific VSMCs are selectively vulnerable to *NOTCH3* variants in CADASIL

To determine if VSMCs in the brain vasculature have specific susceptibility to the *NOTCH3* variants in CADASIL which change cell behaviour and functions, we differentiated iPSCs into VSMCs via neural crest (NC-SMCs), lateral plate mesoderm (LPM-SMCs), and paraxial mesoderm (PM-SMCs), which represent VSMCs of the brain, the heart, and peripheral, respectively, using established methods[32,44] with modifications (**Figs. 1a**).

We first used a wild-type iPSC line to validate features of the origin-specific iPSC-SMCs. During the course of differentiation, pluripotency markers were downregulated, and developmental lineage-specific markers *TFAPA2* (neural crest), *ISL1* (lateral plate mesoderm), and *TBX6* (paraxial mesoderm) were significantly upregulated at the corresponding progenitor stages (**Fig 1b**). The three sub-types of iPSC-SMCs all expressed VSMC specific markers including *ACTA2*/α-SMA, *CNN1*/calponin, *MYH11*/SMMHC and *TAGLN*/SM22α as determined by RT-qPCR (**Fig. 1b**) and immunofluorescent staining (**Fig. 1c and S1a**). Meanwhile, each type of the VSMCs expressed the corresponding lineage-specific markers: *SEMA3α* and *MEF2c* for NC-SMCs, *ISL1* and *HAND1* for LPM-SMCs, and *HOXA10* and *HOXC6* for PM-SMCs (**Fig. S1b**)[45-47]. Comparing to PM-SMCs, the NC-SMCs and LPM-SMCs had much higher proliferation and migration rates, with the NC-SMCs being the highest, as measured by Ki67 immunofluorescence staining (**Fig. 1d and S2a**) and wound healing assay (**Fig. 1e and S2b**), respectively. In contrast, PM-SMCs exhibited the highest contractility, and the LPM-SMCs were least contractile as measured by collagen I contraction assay (**Fig. 1f**). These behavioural and functional properties of the origin-specific iPSC-VSMCs align well with findings reported on primary VSMCs obtained from various vascular locations[48,49]. Additionally, we found for the first time that the NC-SMCs exhibited the highest number of focal adhesions, followed by the LPM-SMCs, as measured by vinculin staining (**Fig. 1g**), suggesting a more active interaction between VSMCs and the matrix in the vasculature of the CNS. PM-SMCs displayed the least number of focal adhesions (**Fig. 1g**).

Having validated the identity of the lineage-specific iPSC-VSMCs, we compared the behaviour and basic functionalities between VSMCs derived from iPSCs of two CADASIL patients (R153C and C224Y) and their corresponding isogenic controls (isoCtrls) that we have made recently using CRISPR/Cas9 gene editing (**Fig. S3**). Cell proliferation as determined by Ki67 staining revealed a significant increase in NC-SMCs derived from the two CADASIL iPSC lines as compared to their isogenic controls (**Fig. 2a**). Interestingly, neither LPM-SMCs nor PM-SMCs from the two CADASIL iPSC lines had significantly altered their proliferation rate, suggesting a specific change in brain VSMCs in CADASIL. Cell migration was conducted using the IncyCyte wound healing assay, revealing again that the CADASIL NC-SMCs, but not the LPM-SMCs nor PM-SMCs, had significantly increased migration compared to the isoCtrls (**Fig. 2b and S4**), further suggesting a selective susceptibility of CNS VSMCs to the CADASIL *NOTCH3* variants.

In addition to the behavioural changes, CADASIL NC-SMCs exhibited significantly impaired contractile function in the collagen I gel contraction assay, unlike the LPS-SMCs and PM-SMCs that showed no difference from their isogenic controls (**Fig. 2c**). Vinculin immunostaining revealed increased but disorganised focal adhesions in CADASIL NC-SMCs, along with diffused cytosolic vinculin signals (**Fig. 2d**), suggesting potential defects in vinculin activation and membrane recruitment[50,51], likely disrupting cytoskeletal organisation[52].

Taken together, results from comparing the behaviour and function of the developmental lineage-specific VSMCs derived from iPSCs strongly suggest a brain-specific vascular vulnerability to the CADASIL *NOTCH3* variants (**Fig. 2**). In the following experiments, the iPSC NC-SMCs model, namely iVSMCs, was exclusively used to study disease mechanisms.

**CADASIL iVSMCs undergo phenotype switching from contractile to synthetic state**

To gain a more comprehensive understanding of genes and signalling pathways that are involved in the pathological changes in CADASIL and identify novel disease mechanisms and therapeutic targets, we conducted bulk RNA sequencing (RNAseq) on NC-SMCs differentiated from two CADASIL iPSC lines (R153C and C224Y), two isogenic control lines (R153C_isoCtrl and C224Y_isoCtrl), and three wild-type control lines (02C9, 02C3 and EIPL1). Principal component analysis (PCA) showed that PC1 explained 67% of the variability that mainly distinguished the CADASIL samples from all the controls (**Fig. 3a**). Differential expression analysis revealed 4161 differentially expressed genes (p-value < 0.05 & $Log_2^{(Fold\ change)} > 1$), including 1932 upregulated and 2229 downregulated genes, between the CADASIL and control samples (**Fig. 3b**). As the isoCtrls and wild-type controls clustered well together on the PCA plot (**Fig. 3a**), thus, only the isogenic controls were used in the subsequent data analysis in order to more accurately identify the impact by the *NOTCH3* variants and avoid the influence by inter-person variations (**Fig. 3c**). Gene ontology (GO) analysis on GO terms of biological process (BP), cellular components (CC) and molecular function (MF) highlighted changes including extracellular matrix organisation, focal adhesion, smooth muscle cell proliferation, smooth cell migration, cell-matrix adhesion, actin filament organisation, collagen-containing extracellular matrix, and regulation of vasculature development (**Fig. 3d**), suggesting a matrix related pathology and phenotype change of CADASIL VSMCs.

We then specifically analysed VSMC phenotype (**Fig. 4a**) on the iPSC CADASIL model. Heatmap of the RNAseq data shows downregulation of a range of contractile marker genes including *MYH11*, *ACTA2*, *CNN1*, *TAGLN,* and *MYOCD*, and upregulation of many synthetic marker genes including *COL1A2*, *MMP9*, *SPP1*, *MYH10*, and *MSN* in the CADASIL iVSMCs (**Fig. 4b**) comparing to isoCtrls, which was confirmed by RT-qPCR (**Fig. 4c**). The downregulation of key contractile markers, α-SMA, MLCK, calponin, and SM22- α, in CADASIL iVSMCs were also confirmed by western blotting (**Fig. 4d**). A chord diagram shows downregulation of a range of genes that linked to GO terms of actin filament binding and muscle cell contraction (**Fig. 4e**). Increased proliferation and migration and reduced contractility are functional features of synthetic VSMCs[36], which we have demonstrated on CADASIL iVSMCs above in **Fig. 2**. Additional migration assay was conducted using 3D VSMC spheroids, further confirming the increased migration of CADASIL iVSMCs (**Fig. S5)**. Taken together, results from gene expressions, protein levels and functional assays suggest that CADASIL iVSMCs undergo phenotype switching from a contractile to a synthetic state.

**ECM composition and adhesion-actin coupling are severely disrupted in CADASIL iVSMCs leading to cell death**

Under the gene ontology (GO) term “extracellular matrix organisation (p = 3.49E-24)”, there were around 150 differentially expressed between the CADASIL iPSC-NC-SMCs and isogenic controls as shown on the heatmap (**Fig. S6a**). Out of the 150 genes, 43 genes were identified to be collagen related, with the majority of which were upregulated (**Fig. S6b**). We then conducted Gene Set Enrichment Analysis (GSEA) to uncover the coordinated change of genes involved in ECM function. GSEA revealed that gene sets relating to “ECM structural constituent”, “collagen biosynthesis and modifying enzymes”, and “collagen trimer” were positively enriched in the CADASIL iVSMCs (**Fig. 5a**), suggesting matrix accumulation and its abnormal turnover in CADASIL. RT-qPCR results confirmed the significant upregulation of key basement membrane components including collagen subtypes (*COL4A2, COL1A1, COL1A2, COL2A1* and *COL3A1*), MMP (*MMP9*), TIMPs (*TIMP1* and *TIMP3*), and *FN* (fibronectin) in the CADASIL iVSMCs comparing to isoCtrls (**Fig. 5b**). Interestingly, MMP3 was consistently found downregulated in the CADASIL iVSMCs (**Fig. 5b**). Considering the unique role of MMP3 that has much broader ECM substrates, including fibronectin and proteoglycans apart from collagens, than other MMPs and participates in proMMP activations[53], the reduced MMP3 may play a significant role in the ECM remodelling in CADASIL. Consistent with the transcriptomic and RT-qPCR results, spheroids formed from CADASIL iVSMCs displayed collagen IV accumulation (**Fig. 5c**). TEM images revealed large amount of matrix deposition (**Fig. 5d**), which is consistent with findings on autopsy samples of human patient [54]. Accompanied with the matrix deposition, accumulation of Notch3 extracellular domain proteins, the hallmark of CADASIL pathology, was also faithfully recapitulated on the iVSMC spheroids (**Fig. 5e**) and western blotting (**Fig. 5f**). Despite accumulation, the mutant Notch3 had impaired CBF1/RBPJκ-mediated canonical Notch activity as determined by luciferase assay (**Fig. S7**).

KEGG analysis highlighted pathways relating to “cytoskeleton in muscle cells”, “focal adhesion”, “regulation of cytoskeleton”, “cell adhesion molecules”, and “ECM-receptor interaction” (**Fig. 6a**), suggesting changes in focal adhesion-actin coupling in CADASIL iVSMCs. Key components of focal adhesion include integrins, tailin, vinculin, paxillin, and focal adhesion kinase (FAK), which link actin cytoskeleton to ECM via integrins (**Fig. 6b**), playing a crucial role in cell-matrix interaction regulating cell behaviours and survival. We then quantified the expression of a range of integrin subunits (*ITGA1, ITGA2, ITGA3, ITGA4, ITGA5, ITGA6, ITGA7, ITGB1, ITGB3*) in the iVSMCs using RT-qPCR and found all of which were significantly downregulated in the CADASIL iPSC-NC-SMCs, except for *ITGA4* that was upregulated in the mutant cells (**Fig. 6c**). Western blotting demonstrated significant reduction in total FAK and pFAK as well as pFAK/FAK ratio in the CADASIL iVSMCs (**Fig. 6d**), suggesting a likely disruption of cell-matrix interaction which compromises cell survival[55]. Fluorescent staining of F-actin cytoskeleton revealed disorganised actin fibre (**Fig. 6e**). To quantify this abnormality, we developed a computer vision algorithm based on Canny edge detection and measures of the disorder of samples, which demonstrated a significantly altered spatial dispersion of actin filaments in the CADASIL iVSMCs as compared to the isoCtrls (**Fig. 6f**), implicating compromised contractility, which is in line with the damaged contractile function (**Fig. 2c**) and reduced contractile markers (**Fig. 4**) in CADASIL iVSMCs as described earlier. Additionally, GSEA showed significantly negative enrichment of “adherence junction” gene sets (**Fig. 6g**), suggesting additional defect in cell-cell interactions. This is also revealed on the TEM images, where smooth lines of cell membranes were observed between adjacent isoCtrl iVSMCs, which was hardly seen in the CADASIL iVSMCs (**Fig. 5d**). Instead, large amounts of cell debris and matrix were frequently observed between adjacent CADASIL iVSMCs (**Fig. 5d**). Taken together, our evidence on the disruption of interactions between both cell-to-matrix and cell-

to-cell suggests a loss of cell anchorage, likely leading to *anoikis*[56]. Indeed, live/dead assay demonstrated a significant increase of cell death in the CADASIL iVSMCs (**Figs. 6h and 6i**). *IGTA4* has specific role in leukocyte adhesion and ECM remodelling in a form of α4β1[57], the upregulation of which (**Fig. 6c**) warrants further investigation.

### Nitric oxide signalling is impaired in CADASIL iVSMCs

KEGG analysis of the RNAseq data highlighted the "cGMP-PKG signalling pathway" (**Fig. 6a**). Given the fact that we had already observed reduced *GUCY1A1* (guanylate cyclase 1 subunit alpha 1 / GCSα1) and *GUCY1B1* (guanylate cyclase 1 subunit beta 1 / sGCβ1) in CADASIL iVSMCs (**Fig. 7b-c**) before the RNAseq screening and the prior knowledge of the profound effects of NO in the regulation of VSMC contractility, proliferation, migration, ECM synthesis, and phenotype switching[58-60], we further explored the involvement of the NO-sGC-cGMP-PKG signalling (**Fig. 7a**) in VSMC pathology of CADASIL. We detected considerable levels of NO in the control iVSMCs with the absence of endothelial cells as measured by DAF-AM staining, which were significantly reduced in the CADASIL iVSMCs (**Fig. 7d**). GCSα1 and GCSβ1 are the two subunits of soluble guanylate cyclase (sGC) that is the primary receptor of NO, which catalyse the synthesis of second messenger cGMP that activate protein kinase G (PKG) inducing VSMC dilation largely via vasodilator-stimulated phosphoprotein (VASP) (**Fig. 7a**)[61,62]. The expression of *PRKG1* and *VASP* and the protein level of VASP were significantly downregulated in CADASIL iVSMCs (**Fig. 7e-f**). To understand the mechanism underlying the reduced NO in CADASIL iVSMCs, we found that endothelial nitric oxide synthase (eNOS) and AKT, a crucial activator of eNOS, were significantly reduced in CADASIL iVSMCs (**Fig. 7g**), while the inducible NOS (iNOS) remained unchanged (**Fig. S8**). eNOS is primarily localised in the plasma membrane and Golgi apparitors, which plays an important role in regulating its enzymatic activity and the bioavailability of NO[63]. We performed immunofluorescence staining and found strikingly that location patterns of eNOS were very different between the CADASIL and isoCtrl iVSMCs. The eNOS signals in the control cells seem associated with intracellular membrane structures, patterns of Golgi and endoplasmic reticulum (ER), whereas the signals in the mutant cells were very weak and defused in cytosol (**Fig. 7h**). As Golgi localisation of eNOS is essential for its posttranslational modifications and activation, the finding likely underlies the compromised NO production (**Fig. 7d**) in CADASIL iVSMCs. Taken together, our results suggest the importance of a local NO-sGC-cGMP signalling in VSMCs independent of ECs, which was dysregulated in CADASIL iVSMCs.

### Treatment of iPSC CADASIL models by PDE5 inhibitor and NO donor significantly restored VSMC function

Building upon our findings, we explored therapeutic potentials by boosting the NO-sGC-cGMP signalling pathway to rescue the key pathological phenotypes of CADASIL iVSMCs. As proof-of-concept experiments, we first supplemented S-nitroso-N-acetylpenicillamine (SNAP), a synthetic NO donor that releases NO under physiological conditions, in cell culture and found that it significantly reversed the abnormal proliferation of CADASIL iVSMCs (**Fig. 8a, 8b** & **S9a**) and moralised protein levels of GCSα1 and GCSβ1 (**Fig. 8d**). However, NO donors usually have short half-life and more suitable in acute settings. To achieve prolonged activation of NO signalling to benefit CADASIL patients and also based on the significant but mild reduction of cGC (*GUCY1A1* and *GUCY1B1*, **Fig. 7c**) in CADASIL iVSMCs, we applied the FDA approved PDE5 inhibitor, sildenafil, that prevents the breakdown of sGC-generated cGMP and activates endogenous sGC-cGMP signalling[64]. Results showed that sildenafil successfully reversed the hyperproliferation of CADASIL iVSMCs to the level of the isogenic

controls (**Fig. 8a, 8c** & **S9a**). The treatments also significantly increased the expression of contractile markers α-SMA and calponin in the CADASIL iVSMCs (**Fig. 8e**). Interestingly, the disorganised actin cytoskeleton in CADASIL iVSMCs were significantly normalised by both SNAP and sildenafil treatments (**Fig. 8f** & **S9b**). Most importantly, both SNAP and sildenafil successfully prevented the cell death of the CADASIL iVSMCs (**Fig. 8g** & **S9c**).

We previously reported that the CADASIL iVSMCs failed to stabilise the capillary tubule structure formed by ECs with a mechanisms of reduced VEGF secretion form the mutant VSMCs[42]. Considering the role of NO in promoting VEGF synthesis in VSMCs [65], we applied SNAP and sildenafil, respectively, during *in vitro* angiogenesis assay, which significantly prolonged the EC tubules stability (**Fig. 9, S10** & **S11**). Our results suggest a promising treatment of CADASIL patients by PDE5 inhibitors to rescue VSMC function and prevent their degeneration seen in CADASIL small vessels.

## Discussion

Using an iPSC model of CADASIL, we uncovered for the first time that iPSC derived VSMCs via a developmental pathway mimicking VSMCs of cerebral vasculature exhibited a unique susceptibility to CADASIL-associated *NOTCH3* mutations, comparing to iPSC-SMCs that mimic sources of peripheral vasculatures. The CADASIL iVSMCs displayed hyperproliferation, hypermigration, reduced contractility, and abnormal cell-matrix interaction. This study also provided the first comprehensive and systemic evaluation of VSMC phenotype in CADASIL, revealing a switching of CADASIL iVSMCs from a contractile to a synthetic phenotype and reinforcing the role of ECM disorganisation in CADASIL pathology. Additionally, we provided evidence of disrupted cell-matrix and cell-cell adhesion of CADASIL iVSMCs, which likely leads to a loss of cell anchorage and subsequent *anoikis*. Finally, alterations in the VSMC-specific NO-sGC-cGMP signalling and phenotype rescue of CADASIL iVSMCs by PDE5 inhibitor, sildenafil, highlight a potential novel therapeutic avenue for CADASIL.

It has been intriguing that CADASIL, a systemic vasculopathy, has prominent manifestations in the brain leading to strokes and vascular dementia while rarely primarily presented as myocardial infarction or symptoms of peripheral vessel disease. Our findings revealed a selective vulnerability of the CADASIL NC-SMCs compared to the LPM-SMCs and PM-SMCs, offering a potential explanation of the paradox. Developmental origin-specific VSMCs exhibit distinct functionalities, including differences in growth behaviours and responses to stimuli[28-30,48,49,66,67]. These differences are intrinsic and driven by unique gene expression profiles including the differential expressed *HOX* genes in lineage-specific VSMCs[47,68-70]. For example, in a mouse model, when vessels prone to atherosclerosis were grafted to abdominal aorta, they developed atherosclerosis in the absence of mechanical and haemodynamic factors[71], highlighting a location-specific tissue susceptibility to disease. Different reactivities of VSMC subtypes to stimulations by growth factors or cytokines likely underlie different disease susceptibility in vessel beds of different locations. Angiotensin II was found to promote proliferation of VSMCs isolated from ascending aorta but not from other aorta regions, whereas PDGF-BB promoted proliferation in VSMCs from all aortic regions[29]. Additionally, TGF-β1 preferentially stimulated the growth and proliferation of neural crest derived VSMCs over mesoderm derived VSMCs via c-myb[30,66] , and interestingly, the former resulted in marked elevation of α1 collagen and the latter had no effect on the α1 collagen gene expression[30]. Based on these observations, it is not surprising to see a selective susceptibility of the cerebral VSMCs to the *NOTCH3* mutations in CADASIL. Our finding is in line with a

pathological report on a postmortem CADASIL patient where minimal changes were observed in liver, spleen, heart and lung whereas significant VSMC disruptions were observed in all small arterioles and capillaries in the brain sample[54].

It is worth noting that what we identified was the vulnerability of the brain VSMCs to CADASIL *NOTCH3* variants which altered key functionalities of the mutant VSMCs, i.e., proliferation, migration, cell-matrix interaction, and contraction. This does not exclude the possibility of peripheral VSMCs developing pathological changes via alternative mechanisms or in a later stage. This also should not override the systemic GOM deposition and Notch3 accumulation that is largely attribute to the conformational change of mutant Notch3 proteins due to cysteine alterations[72]. Nevertheless, the increased sensitivity of brain VSMCs to *NOTCH3* variants likely accelerate the CNS phenotype in CADASIL, suggesting early intervention could benefit CADASIL patients. As our experiments were mostly conducted on 2D monolayer cell cultures, which is difficult for GOM or Notch3 to accumulate, it is therefore attempt to speculate that functional changes reported in isolated primary peripheral VSMCs from CADASIL patients or animal models could mainly attribute to protein accumulations that are systemic. It would be interesting to clarify this as it has not been convincing evidence on whether GOM or Notch3 accumulation are the primary driver of the CADASIL pathology or a secondary effect or readout of the pathology. Overall, our finding contributes to refine future therapeutic targets to cerebral vasculatures for CADASIL and also highlights the importance of using correct models in studying human disease with iPSCs. Future study is to clarify the molecular mechanisms by which *NOTCH3* variants specifically alter the functionality of cerebral VSMCs.

Findings from previous studies on increased proliferation of VSMCs from CADASIL patients[39] and matrix deposition in small arteries of CADASIL mice[73] suggested a phenotype change of VSMCs. However, there have not been studies specifically addressing the VSMC phenotype in CADASIL. Through a comprehensive analysis of transcriptomic data, RT-qPCR, western blotting, immunofluorescent images, and functional assays, we concluded that CADASIL iPSC-SMCs switched from a contractile to synthetic phenotype. The CADASIL iVSMCs highly expressed a set of synthetic markers, decreased expression of contractile related genes, as well as reduced contractility and enhanced proliferation and migration, compared to isogenic controls. Synthetic VSMCs exhibit a secretory feature, which would contribute to the ECM accumulation found in CADASIL arteries. However, the accumulation and disorganised ECM may play an even significant role in driving VSMCs to switch their phenotype. ECM is equally important as growth factors in regulating VSMC phenotypes through binding to their integrin receptors[36,74]. We have found downregulation of a range of integrin genes expressed in the CADASIL iVSMCs, which likely contributed to the VSMC phenotype change. We believe that a vicious cycle is formed where synthetic VSMCs abnormally produce matrix whereas accumulated matrix drives VSMC phenotype changes. Since phenotype switching is a hallmark of atherosclerosis, a target for actively developing therapeutic approaches including those involving non-coding RNAs[75,76], highlighting VSMC phenotype switching in CADASIL could provide opportunities to repurpose treatments originally developed for more common conditions.

It was observed in early year CADASIL research that VSMCs from both human CADASIL patients or mouse models lost anchorage to adjacent cells and ECM, from which it was hypothesised that this might be one of the key events initiating the cascade leading to VSMC degeneration in CADASIL[54,77]. In light of the essential role of integrin-ECM engagement in generating pro-survival signals through activation of FAK and the subsequent recruitment of

vinculin and the focal adhesion formation[78-82], our finding of the significant reduction of FAK, pFAK, and integrins as well as disorganised vinculin in CADASIL iVSMCs provided molecular basis supporting the hypothesis. GESA enriched “adherence junctions” and “cell junction organisation” as well as TEM imaging further support the loss of cell-cell interaction. Abnormal cell-matrix and cell-cell adhesions usually lead to *anoikis*, a type of apoptosis induced by cell detachment[56,78,83]. Indeed, we observed significant level of cell death (**Fig. 6h**) and increased apoptosis in our previous finding[42]. Thus, the CADASIL iPSCs could be a useful human model for future drug discovery aiming to reverse VSMC survival in this condition.

We provided several lines of evidence demonstrating a significant impairment of NO-sGC-cGMP-PKG pathway in CADASIL iVSMCs (**Fig. 7**). For the first time we observed a reduced NO level in the CADASIL iVSMCs. This highlighted a NO-sGC-cGMP-PKG signalling pathway in VSMCs [84-86] with the absence of ECs that usually provide NO for VSMCs for vessel dilatation. While Akt is usually responsible for the phosphorylation and activation of eNOS in ECs, but we identified for the first time that Akt and pAkt were significantly reduced in the CADASIL iVSMCs, which likely contributes to the reduction of NO. Translocation to the Golgi apparatus is required for eNOS palmitoylation, which is essential for eNOS to recycle back to cell membrane caveolae to be activated by Akt[63]. The abnormal location and reduced level of eNOS could affect its activation further reducing NO levels in the CADASIL iVSMCs. Consequently, the NO receptor, sGC subunits, were downregulated at both gene (*GUCY1A1* and *GUCY1B1*) and protein levels, and cGMP effector PKG and VASP were reduced. However, the reduced expression of *GUCY1A1* and *GUCY1B1* could via other mechanisms. It has previously reported an RBP-Jκ binding site on the *GUCY1A3* promoter region in the developing heart[87], linking the canonical Notch signalling to the regulation of sGC. Therefore, the reduced activity of mutant Notch3 (**Fig. S8**), although mild, may partially contribute to the downregulation of *GUCY1A3* in CADASIL VSMCs. Our finding is in line with a previous report where cGMP was reduced in VSMCs from CADASIL mice and patients, although it was caused by oxidation of sGCβ1[88].

To target the damaged NO-sGC-cGMP signalling pathway, we demonstrated that both NO donor SNAP and PDE5 inhibitor Sildenafil could effectively rescue the expression of contractile markers, the abnormal proliferation and angiogenesis, and cell death in the CADASIL iVSMCs. PDE5 specifically targets cellular cGMP for its degradation[64]. Sildenafil, an FDA approved medicine primarily for the treatment of erectile dysfunction, is a PDE5-specific inhibitor augmenting the NO-sGC-cGMP signalling. Although there are controversial findings about the effect of NO on VSMC proliferation, migration and phenotype switching[59], general understanding support a protective role of NO on VSMCs behaviours and functions[58,60,89]. Sildenafil also rescued the impaired function of iVSMCs in stabilising angiogenesis structures which was found in our previous report involving reduced VEGF secretion from the mutant mural cells[42]. It is already known that NO induces the synthesis of VEGF in VSMCs[65] and endogenous NO from endothelial cells promoted angiogenesis[90]. Interestingly, sildenafil has already been found to promote angiogenesis [64,91,92] and upregulate VEGF[93]. All these findings support our results.

To date, accumulating evidence has demonstrated beneficial effects of PDE5 inhibitors in the treatment of a range common conditions including myocardial infarction, cardiac hypertrophy, heart failure, diabetes, cancer, Duchenne muscular dystrophy, Alzheimer’s disease, and aging-related conditions[64]. Most interestingly, a recent work based on a retrospective case-control pharmacoepidemiologic analyses of insurance claims data that included 7.23 million

individuals revealed that sildenafil usage was associated with a 69% reduction of Alzheimer's disease risk[94]. This finding is highly encouraging in relation to our findings in the vascular dementia CADASIL. It has been found that PDE5 exists not only in vascular cells but also in human neurons, which provide a viable target for neurologic disease[90]. Indeed, PDE5 inhibition rescued the oligomeric form of tau protein induced reduction of long-term potentiation and memory impairment[64,95]. New PDE5 inhibitors have been actively developing with a hope to improve its potency, selectivity and BBB permeability[64,96]. The beneficial roles of PDE5 inhibition on both vascular and neurologic functions make it a good candidate for vascular dementia. Therefore, our finding represents a novel but viable treatment for CADASIL, which likely benefit from the drug development for Alzheimer's disease in this area in the future.

Recently, the U.S. Food and Drug Administration (FDA) passed the Modernization Act 3.0, which eliminated the mandate requirement for animal testing and allowed human cell models to be used in preclinical drug development[97,98]. This not only reduces the reliance on animal experimentation, but also greatly encourages the use of iPSC models in human disease research. Our study demonstrated a robust iPSC CADASIL model, which can be used to further investigate disease mechanisms and facilitate drug development, ultimately benefit patients.

## Methods:

### Cell culture

The human induced pluripotent stem cell (iPSC) lines derived from two CADASIL patients carrying the *NOTCH3* heterozygous variants R153C and C224Y and healthy controls, respectively, were reported in our previous studies with local ethical approval (REC reference no. 12/NW/0533)[42,43]. Isogenic control lines (R153C_iso and C224Y_iso) were created using CRISPR/Cas9 gene editing. IPSCs were maintained in Essential 8 medium (Gibco; A1517001) in $CO_2$ incubator at 37°C. For passaging, sub-confluent iPSCs were dissociated using 0.5 mM EDTA (Invitrogen; AM9260G) in PBS at 37 °C for 5–6 minutes. Cells were gently rinsed by pipetting in 1 mL of Essential 8 medium, yielding small aggregates which were seeded onto vitronectin (VTN; 0.005mg/ml; Gibco; A14700)-coated plates at a density of 2.5–3 × $10^3$ cells/cm² in Essential 8 medium supplemented with 10 μM Y-27632 (Tocris; 1254). After 24 hours, the medium was replaced with fresh Essential 8 medium without Y-27632.

### Lineage-specific vascular smooth muscle cell (VSMC) differentiation from iPSCs

Differentiation of VSMCs from iPSCs were performed according to published methods[32,99] with minor modifications.

*Neural crest cell differentiation*. To generate neural crest progenitor cells, iPSCs were cultured on VTN-coated plates in chemically defined Essential 6 medium (Gibco; A1516401) with 10 ng/mL FGF2 (PeproTech; 100-18B) and 10 μM SB431542 (Tocris; 1614). Cells were first passaged at day 5 and subsequently upon reaching confluence, with continued supplementation of FGF2 and SB431542, up to passage 12.

*Mesodermal progenitor cell differentiation*. To induce early mesoderm, human iPSCs were cultured in Essential 6 medium supplemented with 20 ng/mL FGF2, 10 uM LY294002 (Selleckchem; S1105) and 25 ng/mL BMP4 (PeproTech; 120-05ET) for 48 hours. Subsequent mesodermal subtype specification was directed over the following 4 days. Lateral plate mesoderm (LPM) differentiation was achieved by continued exposure to 20 ng/mL FGF2 and

50 ng/mL BMP4, while paraxial mesoderm (PM) differentiation was promoted using 20 ng/mL FGF2 and 10 μM LY294002.

*VSMC differentiation from neural crest cells and mesodermal progenitors.* Following the generation of intermediate populations, cells were trypsinized and cultured in SMC differentiation medium composed of Essential 6 supplemented with 10 ng/mL PDGF-BB (PeproTech; 100-14B) and 2 ng/mL TGF-β1 (PeproTech; 100-21) for a minimum of 12 days. Neural crest-derived VSMCs (NC-SMCs) reached maturity by day18, while LPM- and PM-derived SMCs matured by day 16. These mature iPSC-derived lineage specific VSMCs (iPSC-VSMCs) were subsequently maintained in Smooth Muscle Cell Growth Medium 2 (SMCG2; PromoCell; C-22062) for long-term culture, up to 5 passages.

**Cell proliferation analysis**

Cell proliferation was evaluated by Ki67 immunostaining assay. Mature iPSC-VSMCs were seeded on VTN-coated 24-swell plates at Day 16 for NC-SMCs and Day14 for LPM- and PM-SMCs. After 48 hours interval, cells were fixed with 4% paraformaldehyde (PFA; Thermo Fisher; J61899.AK) and subjected to immunostaining for the proliferation marker Ki67 (Abcam; ab15580). The percentage of Ki67-positive cells was quantified using ImageJ software, based on analysis of at least six randomly selected fields per condition in each experiment. The experiment was independently repeated using iPSC-VSMCs derived from three separate rounds of differentiation

**Cell migration assay**

The migratory behaviour of iPSC-VSMCs was assessed by the wound healing assay using the IncuCyte live-cell imaging system (Sartorius; Essen Bioscience). Mature iPSC-VSMCs ($4X10^4$ cells/well) were seeded onto VTN-coated 96-well ImageLock tissue culture plate (Essen Bioscience) and incubated at 37 °C with 5% $CO_2$ 24 hours to allow cell attachment and confluence. Wounds were introduced by 96-well WoundMaker (Essen Bioscience), followed by two gentle PBS washes to remove detached cells. Wound closure was monitored in real-time by capturing images at 2-hour intervals. Migration was quantified based on changes in wound confluence over time using the IncuCyte analysis software (Essen BioScience). Each condition was tested in technical duplicate, and the experiment was independently repeated using iPSC-VSMCs derived from three separate differentiations

**Collagen-I contraction assay**

Contractile function of iPSC-VSMCs was investigated by collagen I gel contraction assay. The mature iPSC-VSMCs ($1X10^5$ cells/well) were re-suspended and mixed with 150μL of PureCol collagen solution (Advanced Biomatrix; 5005) per well. The collagen-cell suspension was dispensed into 48-well tissue culture plates and allowed to polymerise for an hour at 37 °C. After polymerisation, the gels were mechanically released by gently running a sterile spatula around the well perimeter, followed by a brief flush with medium to ensure complete detachment. Gel contraction was monitored, and images were captured at 48 hours using a ChemiDoc XRS imaging system (Bio-Rad). The area of each gel was quantified using ImageJ software to assess contraction. For each condition, three technical replicates were included, and the experiment was repeated three times using iPSC-VSMCs derived from independent differentiation batches.

**Measurement of intracellular NO levels**

Intracellular nitric oxide (NO) levels in NC-SMCs derived from CADASIL patients and isoCtrls was measured using fluorescent probe 4-amino-5-methylamino-2′,7′-difluorofluorescein

diacetate (DAF-FM; Invitrogen; D23844). Mature NC-SMCs were incubated with 10 µM DAF-FM diacetate in cell culture medium for 30 min at 37 °. Following probe loading, cells were washed with PBS and incubated in fresh medium for another 30 min to allow complete intracellular de-esterification. Fluorescence was visualised using an EVOS M3000 microscope with 488 nm excitation. Quantification of fluorescence intensity was performed using ImageJ, with integrated density measurements was quantified using ImageJ. Images were acquired from five randomly selected fields per condition, and experiments were conducted in triplicate using NC-SMCs obtained from three independent differentiations.

**Cell viability assay**

Cell survival of NC-SMCs from CADASIL patients, isoCtrls, and those treated with activators of the NO–cGMP–PKG signalling pathway was assessed using the LIVE/DEAD Cell Imaging Kit (488/570; Invitrogen; R37601). Mature NC-SMCs were cultured in 24-well plate and cultured for 48 hours at 37 °C in a 5% incubator to make cell recovery. Cells were stained according to the manufacturer's instructions, together with counterstaining Hoechst 33342 (300ng/ml) to label the nuclei. Fluorescent images were acquired using the EVOS M3000 imaging system (Thermo Fisher) with excitation at 488 nm (live cells) and 570 nm (dead cells). Cell viability was calculated as the ratio of live cells to total cells (live + dead) based on Hoechst-positive nuclei. For each condition, five random fields were imaged per well, and the experiment was independently repeated three times using NC-SMCs derived from three separate rounds of differentiation.

**Angiogenesis assay**

The angiogenic response of NC-SMCs from CADASIL patients, isoCtrls, and those treated with activators of the NO–cGMP–PKG signalling pathway was assessed using Matrigel-based endothelial tube formation assay. Growth factor-reduced Matrigel (Corning; 354230) was thawed on ice, dispensed (50 µl/well) into pre-chilled 96-well plates, and incubated overnight at 37 °C in a 5% incubator to allow polymerization. A co-culture of $1.5x10^4$ human umbilical vein endothelial cells (HUVECs) and 0.75 $x10^4$ NC-SMCs was plated onto the thin layer of Matrigel in essential 6 supplemented with 5ng/ml VEGF-165 (PeproTech; 100-20) and 2ng/ml $FGF_2$. Cultures were maintained at 37 °C in a humidified 5% $CO_2$ incubator to promote capillary-like network formation. Tube-like structures were captured at 1, 4, 7, 10, 13, 24, and 48 hours using Brightfield microscopy (EVOS; Thermo Fisher). Quantification of angiogenic parameters, including the number of nodes, total branching length, and total branches length, was performed using imageJ with the "Angiogenesis Analyser" plugin. Each condition was test in technical duplicates, and the experiment was repeated independently three times using iVSMCs derived from three separate rounds of differentiation.

**Generation of spheroids**

Size-matched spheroids were generated by Day 18 NC-SMCs derived from CADASIL patients and isoCtrls using the hanging drop method. Briefly, cells were dissociated with trypsin-EDTA, centrifuged at 300Xg for 5 minutes, re-suspended and counted using an automated cell counter. Approximately $1X10^5$ cells in 20 uL of SMCG2 medium supplemented with 4% poly(vinyl alcohol) (PVA; Sigma-Aldrich; 341584) were seeded per drop. After 24 hours, spheroids were collected and transferred to low attachment 96-well plates. The SMCG2 medium was first replaced at 24 h and subsequently every 48 h for the duration of the culture.

**3D migration assay**

The migratory capacity of NC-SMCs derived from CADASIL patients and isoCtrls was evaluated by 3D spheroid migration assay. For the 3D migration assay, spheroids were cultured for 24 hours and were subsequently embedded in collagen I. The collagen solution was prepared by mixing collagen I matrices (Advanced Biomatrix; 5005) with cell culture medium at a 2:1 ratio, and approximately 300 µL of the mixture was added per well in a 48-well plate. After a 5-minute settling period, 4–5 spheroids were randomly placed into each well. Plates were incubated at 37 °C with 5% $CO_2$ for 1 hour to allow gel polymerization. To inhibit proliferation and focus on cell migration, spheroids were treated with 25 µg/mL mitomycin C (Stemcell Technology; 73274) for 20 min, followed by replacement with fresh culture medium. Brightfield images were acquired daily to monitor spheroid outgrowth. Migration distances were quantified using ImageJ by converting images to 8-bit format with the “Mask” function to enhance visualization and measurement. Each data point in the violin plot represents an individual spheroid. Spheroids were aggregated from NC-SMCs derived from three independent differentiations for biological repeats.

**Transmission Electron Microscope (TEM) protocol for spheroids**

Spheroids were fixed immediately in a solution of 2.5% glutaraldehyde and 4% formaldehyde in 0.1 M HEPES buffer, pH 7.2 2 h. Samples were then rinsed in distilled water. Samples were then post-fixed in a solution of 1.0% osmium tetroxide and 1.5% potassium ferrocyanide in 0.1M cacodylate buffer for 2 h and washed with H2O for 3 times to remove osmium tetroxide residuals. Specimens underwent incubation in thiocarbohydrazide (TCH) for 60 min at RT followed by 5 times washing with distilled water, until any formed TCH crystals are dissolved. Then these spheroids were incubated in 1% osmium tetroxide in distilled water for 1 hour before incubated in 1% uranyl acetate for another an hour.The these specimen underwent dehydration steps in ascending ethanol series (30%, 50 %, 70%, 90%, 100% v/v × 3). Speciment were infiltrated in graded TAAB 812 Hard in acetone at RT overnight. Finally, samples were embedded in free 100% TAAB 812 Hard in labelled mould and put in a stove at 60 °C for 48 h. Ultrathin sections for transmission electron microscopy observations were cut using an ultramicrotome (Leica EM UC6, Vienna, Austria). Ultrathin sections were collected on 100-mesh copper grids (Assing, Rome, Italy) stained with Uranyless© solution and lead citrate 3% solution (Electron Microscopy Science, 1560 Industry Road, Hatfield, PA, USA). Imaging was performed by a transmission electron microscope (Carl Zeiss EM10, Thornwood, NY, USA) set with an accelerating voltage of 60 kV. Images were acquired with a CCD digital camera (AMT CCD, Deben UK Ltd., Suffolk, UK).

**Luciferase reporter assay**

The activation of NOTCH signalling pathway was detected by Dual-Glo Luciferase Assay System (Promega; E2920) as we previously described[21]. The mature NC-SMCs from CADASIL patients and isoCtrls were plated into a 12 well plate and transfected with 4xCSL-luciferase reporter vector (Addgene plasmid 41726,1µg) and Renilla luciferase (0.5µg) using lipofectamine LTX reagent with Plus reagent (Thermo Fisher, 15338030) following the manufacturer’s instructions. After 24 hours of transfection, the activity of firefly luciferase and renilla luciferase were quantified in 96-well plate by a luminometer using Dual-Glo luciferase kit according to the instructions provided by the manufacturer.

**Real-time quantitative polymerase chain reaction**

Cells were harvested from 6-well culture plates, and total RNA was extracted using RNeasy Mini kit (Qiagen; 74104). Then Complementary DNA (cDNA) was synthesized using the high-capacity RNA-to-cDNA kit (Invitrogen; 4388950). Quantitative real-time PCR was performed

using the QuantStudio 6 Real-Time system (Thermo Fisher) using Power SYBR Green PCR Master Mix (Applied Biosystems; 4367659). Gene expression levels were normalized to *GAPDH* as the housekeeping gene, and relative quantification was calculated using the Pfaffl method. Each sample was test in technical triplicate, and the experiment was repeated independently three times using iPSC-VSMCs derived from three separate rounds of differentiation. The primer sequences and efficiency are shown in Table S1.

**Western Blotting**

Cells were lysed with RIPA buffer (Sigma-Aldrich; R0278) supplemented with 100X EDTA-free Halt Protease Inhibitor Cocktail (Thermo Fisher, 87785), and lysates were centrifuged at 16200 x g for 20 min at 4°C. The supernatant was collected, and protein concentration was determined using the Pierce BCA protein assay kit (Thermo Fisher, 23225). For each sample, 20µg of total protein was mixed with NuPAGE LDS sample buffer and β-mercaptoethanol, then boiled at 95°C for 5 min. Proteins were resolved on 12% or 4-20% TGX stain-free precast gels (Bio-rad) and transferred onto nitrocellulose membranes. Membranes were blocked in TBS containing 0.1% (v/v) Tween-20 (TBST) supplemented with 5% (w/v) slim milk powder and 2% (w/v) BSA for an hour at RT, followed by incubation with primary antibodies overnight at 4°C. After washing with TBST, blots were incubated with proper HRP-conjugated secondary antibodies for 2 hours at RT. Signal detection was performed using SuperSignal™ West Pico or Femto Chemiluminescent Substrate (Thermo Fisher Scientific), and blots were imaged using autoradiography. Where indicated, band intensities were quantified by densitometry using Image Lab software (Bio-Rad).

**Immunofluorescence on 3D spheroids**

Immunofluorescence (IF) staining was performed to assess NOTCH3 (R&D; AF1308) and collagen IV (Thermo Fisher; PA5-104508) expression in 3D spheroids derived from NC-SMCs. Spheroids were cultured in SMCG2 medium for an additional 7 days to promote extracellular matrix formation. Subsequently, spheroids were collected into 1.5 ml Eppendorf tubes, washed with PBS, and fixed in 4% PFA for 2 hours at 4°C. Fixed spheroids were permeabilized with 0.5% (v/v) Triton X-100 in PBS for 4 hours at room temperature (RT), followed by blocking overnight in IF buffer containing 10 % donkey serum, 2% (w/v) BSA, 0.2% (v/v) Triton X-100, and 0.05% (v/v) Tween-20 in PBS. Primary anti-human antibodies NOTCH3 and Collagen IV were diluted in fresh IF buffer and incubated the spheroids for 3 days at RT. After primary incubation, spheroids were washed 3 times with IF buffer and incubated for 24 hours at RT with species-specific secondary antibodies (anti-goat Alexa Fluor 488 and anti-rabbit Alexa Fluor 647) and Hoechst 33342 (1:50,000 dilution) diluted in IF buffer. Following three additional washes, spheroids were mounted in 0.5 mm deep iSpacer chambers filled with Rapiclear 1.49 (Sunjin Lab Co.). Spheroids were imaged using a Leica SP8 confocal microscope under a 10x objective. Z-stacks were acquired and processed using ImageJ to generate either 2D maximum intensity projections or 3D reconstructions.

**Immunofluorescence on monolayer iPSC-VSMCs**

IF was performed to assess the expression of VSMC-specific or functional markers in iPSC-VSMCs. Cells were cultured on VTN-coated coverslips or 24-well plates and fixed with 4% PFA for 15 minutes at RT. Following fixation, cells were permeabilized with 0.5% Triton X-100 in PBS for 20 min and blocked in IF buffer an hour at RT. Cells were then incubated with primary antibodies: anti-αSMA antibody (1:250, Abcam, ab7817), anti-calponin (1:250, Abcam, ab46794), anti-transgelin (1:500, Abcam, ab14106), anti-vinculin (1:500, Sigma-Aldrich, V9131), anti-eNOS (1:200; Novus, NB300) diluted in IF buffer overnight at RT. After washing,

appropriate Alexa Fluor–conjugated secondary antibodies were applied for two hours at room temperature in darkness. Nuclei were counterstained with DAPI. Coverslips were mounted using Fluoromount-G mounting medium (Invitrogen; 00-4958-02), and images were acquired using a fluorescence or Leica SP8 confocal microscope. Quantification of fluorescence intensity or positive cell percentage was performed using ImageJ.

**F-actin staining and quantification**

Immature NC-SMCs (Day12) were placed onto VTN-coated glass coverslips and cultured in SMC differentiation medium. At day 18, cells were fixed with 4% PFA for 15 minutes at RT, permeabilized with 0.5% Triton X-100 in PBS for 10 minutes, and blocked in IF buffer for 30 minutes. For visualization of the cytoskeletal structure, F-actin was stained using Phalloidin-iFluor 488 Reagent (Abcam, ab176753) for 2 hours at RT. Nuclei were counterstained with DAPI. Images were acquired using a Leica SP8 inverted confocal microscope equipped with a 100× oil immersion objective.

Spatial dispersion is used to quantify cytoskeletal organization. We resize the input image to 512×512 pixels. Then, the standard Canny edge detection algorithm[100] is employed to outline the edges of stress fibres. Firstly, a Gaussian filter is applied to smoothing the image whilst reducing image noise. Afterwards, image gradients are computed so that potential edges can be better identified. The detected edges are then processed using a Non-Maximum Suppression (NMS) technique[101] to eliminate false detections, followed by edge screening via a dual-threshold approach of Canny edge detection[100]. The dual thresholds are determined, based on statistical characteristics of image pixels. To be specific, the standard Sobel operator[102] is used to calculate horizontal (*x*) and vertical (*y*) gradients ($G_x$ and $G_y$). The gradient magnitude *G* at each pixel, representing gradient intensity, is computed as:

$$G=\sqrt{G_x^2+G_y^2}$$

The mean (*M*) and standard deviation (*S*) of the gradient magnitudes are then calculated. The upper threshold ($T_{max}$) and the lower threshold ($T_{min}$) are determined as follows, where T denotes the reduction ratio:

$$T_{max}=M+2\times S$$

$$T_{min}= T_{max}/T$$

Next, the resized image is converted to the counterpart in the HSV colour space. The centre point of the blue region is identified based on a predefined HSV range. For each stress fibre edge, two parameters are computed:

1. The distance ($D^i$) from the centre of the blue region to the edge.

2. The angle ($A^i$) between the edge and the horizontal axis (0° < $A^i$ < 180°).

For the images containing multiple blue regions, the average distance ($D^i_{avg}$) from each stress fibre edge to all the blue centres is calculated individually. During this process, small blue regions and short stress fibre edges are filtered out.

Finally, spatial dispersion (*dsp*) is used to measure the degree of disorder. Each pair ($D^i_{avg}$, $A^i$) is treated as a point in the 2D space. The space is divided into *n* subspaces, and the probability *p* of the points falling into each subspace is computed as the ratio of the points in

that specific subspace against the total number of the points. The entropy (*etp*) and the normalized spatial dispersion (*dsp*) are derived as follows:

$$etp = sum(-p \times \log(p))$$

$$dsp = \frac{etp}{-\log(\frac{1}{n})}$$

where *etp* is used to measure the uncertainty of the point distribution within spatial sub-regions, where *p* represents the proportion of the points in each sub-region relative to the total number of the points. *n* denotes the total number of the sub-regions. By dividing *etp* by the maximum entropy ($\log_2 n$), the result is normalized to a scale of [0,1], facilitating the comparisons across different regions.

This code is available at https://github.com/zhaoaite/ActinDetection.

**RNA-seq sample processing, sequencing and data processing**

Total RNA isolated using the abovementioned method was submitted to the Genomic Technologies Core Facility (GTCF) at the University of Manchester. The quality and integrity of the RNA samples were assessed using a 4200 TapeStation (Agilent Technologies, Cheadle, UK) and then libraries generated using the Illumina® Stranded mRNA Prep. Ligation kit (Illumina, Inc., Cambridge, UK) according to the manufacturer's protocol. Briefly, total RNA (typically 0.025–1µg) was used as input material, from which polyadenylated mRNA was purified using poly-T, oligo-attached, magnetic beads. Next, the mRNA was fragmented under elevated temperature and then reverse transcribed into first-strand cDNA using random hexamer primers and in the presence of Actinomycin D (thus improving strand specificity whilst mitigating spurious DNA-dependent synthesis). Following removal of the template RNA, second-strand cDNA was then synthesised to yield blunt-ended, double-stranded cDNA fragments. Strand specificity was maintained by the incorporation of deoxyuridine triphosphate (dUTP) in place of dTTP to quench the second strand during subsequent amplification. Following a single adenine (A) base addition, adapters with a corresponding, complementary thymine (T) overhang were ligated to the cDNA fragments. Pre-index anchors were then ligated to the ends of the double-stranded cDNA fragments to prepare them for dual indexing. A subsequent PCR amplification step was then used to add the index adapter sequences to create the final cDNA library. The adapter indices enabled the multiplexing of the libraries, which were pooled prior to cluster generation using a cBot instrument. The loaded flow-cell was then paired-end sequenced (76 + 76 cycles, plus indices) on an Illumina HiSeq4000 instrument. Finally, the output data was demultiplexed and BCL-to-Fastq conversion performed using Illumina's bcl2fastq software, version 2.20.0.422 (Illumina, Inc., San Diego, CA, USA)

For RNAseq analysis, the unmapped paired-end sequences from the HiSeq 4000 were assessed by FastQC (http://www.bioinformatics.babraham.ac.uk/projects/fastqc/, accessed on 15 October 2021). Sequence adapters were removed, and reads were quality trimmed to quality q20 using Trimmomatic_0.36 (PMID: 24695404). The reads were mapped against the reference human (hg38) genome and counts per gene were calculated using annotation from GENCODE 30 (http://www.gencodegenes.org/, accessed on 15 October 2021) using STAR_2.5.3a (PMID: 23104886). Downstream normalisation, principal components analysis (PCA) and differential expression were calculated in DESeq2_1.20.0 using default settings (PMID:25516281). Differentially expressed genes (DEGs) were identified between NC-SMCs

derived from CADASIL patients and controls (isoCtrl and wild-type) using an adjusted $p < 0.05$ and $|\log_2(\text{fold change})| > 1$.

Results were visualized using heatmaps generated with the pheatmap package (v1.0.12; R Foundation for Statistical Computing, Vienna, Austria). The volcano plots derived from DESeq2 statistical outputs was plotted by https://www.bioinformatics.com.cn (last accessed on 10 Dec 2024), an online platform for data analysis and visualization.Gene Ontology (GO) and Kyoto Encyclopedia of Genes and Genomes (KEGG) pathway enrichment analyses, as well as Gene Set Enrichment Analysis (GSEA), were conducted using the clusterProfiler package (v3.16.0; Bioconductor, Boston, MA, USA) to characterize biological processes and signalling pathways enriched among significantly upregulated or downregulated genes, and the pictures were plotted by https://www.bioinformatics.com.cn

**Statistical analysis**

All statistical analyses were performed using GraphPad Prism version 10.0 (GraphPad Software, San Diego, CA, USA) and R version 4.4.2 (R Foundation for Statistical Computing, Vienna, Austria). Data are presented as mean ± standard error of the mean (SEM).

The Shapiro-Wilk test was employed to assess the normality of data distributions. For comparison between CADASIL patient and their respective isoCtrls, unpaired Student's t-test was utilised. One-way ANOVA followed by Tukey's post hoc test was applied for multiple comparison amongst the three lineage-specific VSMCs. For experiments involving two independent variables, *NOTCH3* variants and treatment, two-way ANOVA followed by Tukey's multiple comparisons test was conducted to evaluate group differences. A p-value of less than 0.05 was considered statistically significant. All experiments were conducted with a minimum of three biological replicates as three independent rounds of differentiation of each iPSC line. Detailed sample sizes and the number of replicates for each experiment are specified in the corresponding method.

## References:


1. Wardlaw JM, Smith C, Dichgans M. Small vessel disease: mechanisms and clinical implications. *Lancet Neurol*. 2019;18:684-696. doi: 10.1016/S1474-4422(19)30079-1
2. Bordes C, Sargurupremraj M, Mishra A, Debette S. Genetics of common cerebral small vessel disease. *Nat Rev Neurol*. 2022;18:84-101. doi: 10.1038/s41582-021-00592-8
3. Armstrong NJ, Mather KA, Sargurupremraj M, Knol MJ, Malik R, Satizabal CL, Yanek LR, Wen W, Gudnason VG, Dueker ND, et al. Common Genetic Variation Indicates Separate Causes for Periventricular and Deep White Matter Hyperintensities. *Stroke*. 2020;51:2111-2121. doi: 10.1161/STROKEAHA.119.027544
4. Joutel A, Corpechot C, Ducros A, Vahedi K, Chabriat H, Mouton P, Alamowitch S, Domenga V, Cecillion M, Marechal E, et al. Notch3 mutations in CADASIL, a hereditary adult-onset condition causing stroke and dementia. *Nature*. 1996;383:707-710. doi: 10.1038/383707a0
5. Sharma P, Wang T, Brown MJ, Schapira AH. Fits and strokes. *Lancet*. 2001;358:120. doi: 10.1016/S0140-6736(01)05331-4
6. Cho BPH, Nannoni S, Harshfield EL, Tozer D, Graf S, Bell S, Markus HS. NOTCH3 variants are more common than expected in the general population and associated with stroke and vascular dementia: an analysis of 200 000 participants. *J Neurol Neurosurg Psychiatry*. 2021;92:694-701. doi: 10.1136/jnnp-2020-325838

7. Cho BPH, Harshfield EL, Al-Thani M, Tozer DJ, Bell S, Markus HS. Association of Vascular Risk Factors and Genetic Factors With Penetrance of Variants Causing Monogenic Stroke. *JAMA Neurol*. 2022;79:1303-1311. doi: 10.1001/jamaneurol.2022.3832
8. Rutten JW, Dauwerse HG, Gravesteijn G, van Belzen MJ, van der Grond J, Polke JM, Bernal-Quiros M, Lesnik Oberstein SA. Archetypal NOTCH3 mutations frequent in public exome: implications for CADASIL. *Ann Clin Transl Neurol*. 2016;3:844-853. doi: 10.1002/acn3.344
9. Chabriat H, Joutel A, Dichgans M, Tournier-Lasserve E, Bousser MG. Cadasil. *Lancet Neurol*. 2009;8:643-653. doi: 10.1016/S1474-4422(09)70127-9
10. Chabriat H, Joutel A, Tournier-Lasserve E, Bousser MG. CADASIL: yesterday, today, tomorrow. *Eur J Neurol*. 2020;27:1588-1595. doi: 10.1111/ene.14293
11. Dichgans M. Cognition in CADASIL. *Stroke*. 2009;40:S45-47. doi: 10.1161/STROKEAHA.108.534412
12. Romay MC, Knutsen RH, Ma F, Mompeon A, Hernandez GE, Salvador J, Mirkov S, Batra A, Sullivan DP, Procissi D, et al. Age-related loss of Notch3 underlies brain vascular contractility deficiencies, glymphatic dysfunction, and neurodegeneration in mice. *J Clin Invest*. 2024;134. doi: 10.1172/JCI166134
13. Domenga V, Fardoux P, Lacombe P, Monet M, Maciazek J, Krebs LT, Klonjkowski B, Berrou E, Mericskay M, Li Z, et al. Notch3 is required for arterial identity and maturation of vascular smooth muscle cells. *Genes Dev*. 2004;18:2730-2735. doi: 10.1101/gad.308904
14. Wang W, Prince CZ, Mou Y, Pollman MJ. Notch3 signaling in vascular smooth muscle cells induces c-FLIP expression via ERK/MAPK activation. Resistance to Fas ligand-induced apoptosis. *J Biol Chem*. 2002;277:21723-21729. doi: 10.1074/jbc.M202224200
15. Campos AH, Wang W, Pollman MJ, Gibbons GH. Determinants of Notch-3 receptor expression and signaling in vascular smooth muscle cells: implications in cell-cycle regulation. *Circ Res*. 2002;91:999-1006. doi: 10.1161/01.res.0000044944.99984.25
16. Joutel A, Andreux F, Gaulis S, Domenga V, Cecillon M, Battail N, Piga N, Chapon F, Godfrain C, Tournier-Lasserve E. The ectodomain of the Notch3 receptor accumulates within the cerebrovasculature of CADASIL patients. *J Clin Invest*. 2000;105:597-605. doi: 10.1172/JCI8047
17. Joutel A, Vahedi K, Corpechot C, Troesch A, Chabriat H, Vayssiere C, Cruaud C, Maciazek J, Weissenbach J, Bousser MG, et al. Strong clustering and stereotyped nature of Notch3 mutations in CADASIL patients. *Lancet*. 1997;350:1511-1515. doi: 10.1016/S0140-6736(97)08083-5
18. Joutel A, Favrole P, Labauge P, Chabriat H, Lescoat C, Andreux F, Domenga V, Cecillon M, Vahedi K, Ducros A, et al. Skin biopsy immunostaining with a Notch3 monoclonal antibody for CADASIL diagnosis. *Lancet*. 2001;358:2049-2051. doi: 10.1016/S0140-6736(01)07142-2
19. Monet M, Domenga V, Lemaire B, Souilhol C, Langa F, Babinet C, Gridley T, Tournier-Lasserve E, Cohen-Tannoudji M, Joutel A. The archetypal R90C CADASIL-NOTCH3 mutation retains NOTCH3 function in vivo. *Hum Mol Genet*. 2007;16:982-992. doi: 10.1093/hmg/ddm042
20. Hayward P, Kalmar T, Arias AM. Wnt/Notch signalling and information processing during development. *Development*. 2008;135:411-424. doi: 10.1242/dev.000505
21. Wang T, Holt CM, Xu C, Ridley C, R POJ, Baron M, Trump D. Notch3 activation modulates cell growth behaviour and cross-talk to Wnt/TCF signalling pathway. *Cell Signal*. 2007;19:2458-2467. doi: 10.1016/j.cellsig.2007.07.019
22. Rallis G, Koletsa T, Saridaki Z, Manousou K, Koliou GA, Kostopoulos I, Kotoula V, Makatsoris T, Kourea HP, Raptou G, et al. Association of Notch and Hedgehog Pathway Activation With Prognosis in Early-stage Colorectal Cancer. *Anticancer Res*. 2019;39:2129-2138. doi: 10.21873/anticanres.13326

23. Blokzijl A, Dahlqvist C, Reissmann E, Falk A, Moliner A, Lendahl U, Ibanez CF. Cross-talk between the Notch and TGF-beta signaling pathways mediated by interaction of the Notch intracellular domain with Smad3. *J Cell Biol*. 2003;163:723-728. doi: 10.1083/jcb.200305112
24. Gutierrez A, Look AT. NOTCH and PI3K-AKT pathways intertwined. *Cancer Cell*. 2007;12:411-413. doi: 10.1016/j.ccr.2007.10.027
25. Mittal S, Subramanyam D, Dey D, Kumar RV, Rangarajan A. Cooperation of Notch and Ras/MAPK signaling pathways in human breast carcinogenesis. *Mol Cancer*. 2009;8:128. doi: 10.1186/1476-4598-8-128
26. Rippe C, Zhu B, Krawczyk KK, Bavel EV, Albinsson S, Sjolund J, Bakker E, Sward K. Hypertension reduces soluble guanylyl cyclase expression in the mouse aorta via the Notch signaling pathway. *Sci Rep*. 2017;7:1334. doi: 10.1038/s41598-017-01392-1
27. Wang G, Jacquet L, Karamariti E, Xu Q. Origin and differentiation of vascular smooth muscle cells. *J Physiol*. 2015;593:3013-3030. doi: 10.1113/JP270033
28. Bennett MR, Sinha S, Owens GK. Vascular Smooth Muscle Cells in Atherosclerosis. *Circ Res*. 2016;118:692-702. doi: 10.1161/CIRCRESAHA.115.306361
29. Owens AP, 3rd, Subramanian V, Moorleghen JJ, Guo Z, McNamara CA, Cassis LA, Daugherty A. Angiotensin II induces a region-specific hyperplasia of the ascending aorta through regulation of inhibitor of differentiation 3. *Circ Res*. 2010;106:611-619. doi: 10.1161/CIRCRESAHA.109.212837
30. Gadson PF, Jr., Dalton ML, Patterson E, Svoboda DD, Hutchinson L, Schram D, Rosenquist TH. Differential response of mesoderm- and neural crest-derived smooth muscle to TGF-beta1: regulation of c-myb and alpha1 (I) procollagen genes. *Exp Cell Res*. 1997;230:169-180. doi: 10.1006/excr.1996.3398
31. El-Hamamsy I, Yacoub MH. Cellular and molecular mechanisms of thoracic aortic aneurysms. *Nat Rev Cardiol*. 2009;6:771-786. doi: 10.1038/nrcardio.2009.191
32. Granata A, Serrano F, Bernard WG, McNamara M, Low L, Sastry P, Sinha S. An iPSC-derived vascular model of Marfan syndrome identifies key mediators of smooth muscle cell death. *Nat Genet*. 2017;49:97-109. doi: 10.1038/ng.3723
33. VanderLaan PA, Reardon CA, Getz GS. Site specificity of atherosclerosis: site-selective responses to atherosclerotic modulators. *Arterioscler Thromb Vasc Biol*. 2004;24:12-22. doi: 10.1161/01.ATV.0000105054.43931.f0
34. Van Assche T, Hendrickx J, Crauwels HM, Guns PJ, Martinet W, Fransen P, Raes M, Bult H. Transcription profiles of aortic smooth muscle cells from atherosclerosis-prone and -resistant regions in young apolipoprotein E-deficient mice before plaque development. *J Vasc Res*. 2011;48:31-42. doi: 10.1159/000317398
35. Shanahan CM, Weissberg PL. Smooth muscle cell heterogeneity: patterns of gene expression in vascular smooth muscle cells in vitro and in vivo. *Arterioscler Thromb Vasc Biol*. 1998;18:333-338. doi: 10.1161/01.atv.18.3.333
36. Rensen SS, Doevendans PA, van Eys GJ. Regulation and characteristics of vascular smooth muscle cell phenotypic diversity. *Neth Heart J*. 2007;15:100-108. doi: 10.1007/BF03085963
37. Joutel A, Monet-Lepretre M, Gosele C, Baron-Menguy C, Hammes A, Schmidt S, Lemaire-Carrette B, Domenga V, Schedl A, Lacombe P, et al. Cerebrovascular dysfunction and microcirculation rarefaction precede white matter lesions in a mouse genetic model of cerebral ischemic small vessel disease. *J Clin Invest*. 2010;120:433-445. doi: 10.1172/JCI39733
38. Peters N, Freilinger T, Opherk C, Pfefferkorn T, Dichgans M. Enhanced L-arginine-induced vasoreactivity suggests endothelial dysfunction in CADASIL. *J Neurol*. 2008;255:1203-1208. doi: 10.1007/s00415-008-0876-9
39. Neves KB, Harvey AP, Moreton F, Montezano AC, Rios FJ, Alves-Lopes R, Nguyen Dinh Cat A, Rocchiccioli P, Delles C, Joutel A, et al. ER stress and Rho kinase activation underlie the vasculopathy of CADASIL. *JCI Insight*. 2019;4. doi: 10.1172/jci.insight.131344

40. Ayata C. CADASIL: experimental insights from animal models. *Stroke*. 2010;41:S129-134. doi: 10.1161/STROKEAHA.110.595207
41. Sun D, Gao W, Hu H, Zhou S. Why 90% of clinical drug development fails and how to improve it? *Acta Pharm Sin B*. 2022;12:3049-3062. doi: 10.1016/j.apsb.2022.02.002
42. Kelleher J, Dickinson A, Cain S, Hu Y, Bates N, Harvey A, Ren J, Zhang W, Moreton FC, Muir KW, et al. Patient-Specific iPSC Model of a Genetic Vascular Dementia Syndrome Reveals Failure of Mural Cells to Stabilize Capillary Structures. *Stem Cell Reports*. 2019;13:817-831. doi: 10.1016/j.stemcr.2019.10.004
43. Zhang W, Zhao X, Qi X, Kimber SJ, Hooper NM, Wang T. Induced pluripotent stem cell model revealed impaired neurovascular interaction in genetic small vessel disease Cerebral Autosomal Dominant Arteriopathy with Subcortical Infarcts and Leukoencephalopathy. *Front Cell Neurosci*. 2023;17:1195470. doi: 10.3389/fncel.2023.1195470
44. Cheung C, Bernardo AS, Trotter MW, Pedersen RA, Sinha S. Generation of human vascular smooth muscle subtypes provides insight into embryological origin-dependent disease susceptibility. *Nat Biotechnol*. 2012;30:165-173. doi: 10.1038/nbt.2107
45. Wu JH, Zhou YF, Hong CD, Chen AQ, Luo Y, Mao L, Xia YP, He QW, Jin HJ, Huang M, et al. Semaphorin-3A protects against neointimal hyperplasia after vascular injury. *EBioMedicine*. 2019;39:95-108. doi: 10.1016/j.ebiom.2018.12.023
46. Barnes RM, Firulli BA, Conway SJ, Vincentz JW, Firulli AB. Analysis of the Hand1 cell lineage reveals novel contributions to cardiovascular, neural crest, extra-embryonic, and lateral mesoderm derivatives. *Dev Dyn*. 2010;239:3086-3097. doi: 10.1002/dvdy.22428
47. Trigueros-Motos L, Gonzalez-Granado JM, Cheung C, Fernandez P, Sanchez-Cabo F, Dopazo A, Sinha S, Andres V. Embryological-origin-dependent differences in homeobox expression in adult aorta: role in regional phenotypic variability and regulation of NF-kappaB activity. *Arterioscler Thromb Vasc Biol*. 2013;33:1248-1256. doi: 10.1161/ATVBAHA.112.300539
48. Castro C, Diez-Juan A, Cortes MJ, Andres V. Distinct regulation of mitogen-activated protein kinases and p27Kip1 in smooth muscle cells from different vascular beds. A potential role in establishing regional phenotypic variance. *J Biol Chem*. 2003;278:4482-4490. doi: 10.1074/jbc.M204716200
49. Nishiguchi F, Fukui R, Hoshiga M, Negoro N, Ii M, Nakakohji T, Kohbayashi E, Ishihara T, Hanafusa T. Different migratory and proliferative properties of smooth muscle cells of coronary and femoral artery. *Atherosclerosis*. 2003;171:39-47. doi: 10.1016/j.atherosclerosis.2003.08.007
50. Bakolitsa C, Cohen DM, Bankston LA, Bobkov AA, Cadwell GW, Jennings L, Critchley DR, Craig SW, Liddington RC. Structural basis for vinculin activation at sites of cell adhesion. *Nature*. 2004;430:583-586. doi: 10.1038/nature02610
51. Marquez MG, Brandan YR, Guaytima Edel V, Pavan CH, Favale NO, Sterin-Speziale NB. Physiologically induced restructuring of focal adhesions causes mobilization of vinculin by a vesicular endocytic recycling pathway. *Biochim Biophys Acta*. 2014;1843:2991-3003. doi: 10.1016/j.bbamcr.2014.09.014
52. Wang H, Said R, Nguyen-Vigouroux C, Henriot V, Gebhardt P, Pernier J, Grosse R, Le Clainche C. Talin and vinculin combine their activities to trigger actin assembly. *Nat Commun*. 2024;15:9497. doi: 10.1038/s41467-024-53859-1
53. Nagase H, Visse R, Murphy G. Structure and function of matrix metalloproteinases and TIMPs. *Cardiovasc Res*. 2006;69:562-573. doi: 10.1016/j.cardiores.2005.12.002
54. Ruchoux MM, Guerouaou D, Vandenhaute B, Pruvo JP, Vermersch P, Leys D. Systemic vascular smooth muscle cell impairment in cerebral autosomal dominant arteriopathy with subcortical infarcts and leukoencephalopathy. *Acta Neuropathol*. 1995;89:500-512. doi: 10.1007/BF00571504

55. Reyes L, Naser L, Weiner WS, Thifault D, Stahl E, McCreary L, Nott R, Quick C, Buchberger A, Alvarado C, et al. Structure-based discovery of hydrocarbon-stapled paxillin peptides that block FAK scaffolding in cancer. *Nat Commun*. 2025;16:2060. doi: 10.1038/s41467-025-57196-9
56. Taddei ML, Giannoni E, Fiaschi T, Chiarugi P. Anoikis: an emerging hallmark in health and diseases. *J Pathol*. 2012;226:380-393. doi: 10.1002/path.3000
57. Baiula M, Spampinato S, Gentilucci L, Tolomelli A. Novel Ligands Targeting alpha(4)beta(1) Integrin: Therapeutic Applications and Perspectives. *Front Chem*. 2019;7:489. doi: 10.3389/fchem.2019.00489
58. Golshiri K, Ataei Ataabadi E, Portilla Fernandez EC, Jan Danser AH, Roks AJM. The importance of the nitric oxide-cGMP pathway in age-related cardiovascular disease: Focus on phosphodiesterase-1 and soluble guanylate cyclase. *Basic Clin Pharmacol Toxicol*. 2020;127:67-80. doi: 10.1111/bcpt.13319
59. Lehners M, Dobrowinski H, Feil S, Feil R. cGMP Signaling and Vascular Smooth Muscle Cell Plasticity. *J Cardiovasc Dev Dis*. 2018;5. doi: 10.3390/jcdd5020020
60. Lincoln TM, Wu X, Sellak H, Dey N, Choi CS. Regulation of vascular smooth muscle cell phenotype by cyclic GMP and cyclic GMP-dependent protein kinase. *Front Biosci*. 2006;11:356-367. doi: 10.2741/1803
61. Waldmann R, Nieberding M, Walter U. Vasodilator-stimulated protein phosphorylation in platelets is mediated by cAMP- and cGMP-dependent protein kinases. *Eur J Biochem*. 1987;167:441-448. doi: 10.1111/j.1432-1033.1987.tb13357.x
62. Benz PM, Fromel T, Laban H, Zink J, Ulrich L, Groneberg D, Boon RA, Poley P, Renne T, de Wit C, et al. Cardiovascular Functions of Ena/VASP Proteins: Past, Present and Beyond. *Cells*. 2023;12. doi: 10.3390/cells12131740
63. Villadangos L, Serrador JM. Subcellular Localization Guides eNOS Function. *Int J Mol Sci*. 2024;25. doi: 10.3390/ijms252413402
64. Samidurai A, Xi L, Das A, Kukreja RC. Beyond Erectile Dysfunction: cGMP-Specific Phosphodiesterase 5 Inhibitors for Other Clinical Disorders. *Annu Rev Pharmacol Toxicol*. 2023;63:585-615. doi: 10.1146/annurev-pharmtox-040122-034745
65. Dulak J, Jozkowicz A, Dembinska-Kiec A, Guevara I, Zdzienicka A, Zmudzinska-Grochot D, Florek I, Wojtowicz A, Szuba A, Cooke JP. Nitric oxide induces the synthesis of vascular endothelial growth factor by rat vascular smooth muscle cells. *Arterioscler Thromb Vasc Biol*. 2000;20:659-666. doi: 10.1161/01.atv.20.3.659
66. Topouzis S, Majesky MW. Smooth muscle lineage diversity in the chick embryo. Two types of aortic smooth muscle cell differ in growth and receptor-mediated transcriptional responses to transforming growth factor-beta. *Dev Biol*. 1996;178:430-445. doi: 10.1006/dbio.1996.0229
67. Pfaltzgraff ER, Bader DM. Heterogeneity in vascular smooth muscle cell embryonic origin in relation to adult structure, physiology, and disease. *Dev Dyn*. 2015;244:410-416. doi: 10.1002/dvdy.24247
68. Zhang H, Gu S, Al-Sabeq B, Wang S, He J, Tam A, Cifelli C, Mathalone N, Tirgari S, Boyd S, et al. Origin-specific epigenetic program correlates with vascular bed-specific differences in Rgs5 expression. *FASEB J*. 2012;26:181-191. doi: 10.1096/fj.11-185454
69. Pruett ND, Hajdu Z, Zhang J, Visconti RP, Kern MJ, Wellik DM, Majesky MW, Awgulewitsch A. Changing topographic Hox expression in blood vessels results in regionally distinct vessel wall remodeling. *Biol Open*. 2012;1:430-435. doi: 10.1242/bio.2012039
70. Pruett ND, Visconti RP, Jacobs DF, Scholz D, McQuinn T, Sundberg JP, Awgulewitsch A. Evidence for Hox-specified positional identities in adult vasculature. *BMC Dev Biol*. 2008;8:93. doi: 10.1186/1471-213X-8-93
71. Haimovici H, Maier N. Experimental canine atherosclerosis in autogenous abdominal aortic grafts implanted into the jugular vein. *Atherosclerosis*. 1971;13:375-384. doi: 10.1016/0021-9150(71)90080-3

72. Duering M, Karpinska A, Rosner S, Hopfner F, Zechmeister M, Peters N, Kremmer E, Haffner C, Giese A, Dichgans M, et al. Co-aggregate formation of CADASIL-mutant NOTCH3: a single-particle analysis. *Hum Mol Genet*. 2011;20:3256-3265. doi: 10.1093/hmg/ddr237
73. Monet-Lepretre M, Haddad I, Baron-Menguy C, Fouillot-Panchal M, Riani M, Domenga-Denier V, Dussaule C, Cognat E, Vinh J, Joutel A. Abnormal recruitment of extracellular matrix proteins by excess Notch3 ECD: a new pathomechanism in CADASIL. *Brain*. 2013;136:1830-1845. doi: 10.1093/brain/awt092
74. Moiseeva EP. Adhesion receptors of vascular smooth muscle cells and their functions. *Cardiovasc Res*. 2001;52:372-386. doi: 10.1016/s0008-6363(01)00399-6
75. Kansakar U, Jankauskas SS, Gambardella J, Santulli G. Targeting the phenotypic switch of vascular smooth muscle cells to tackle atherosclerosis. *Atherosclerosis*. 2021;324:117-120. doi: 10.1016/j.atherosclerosis.2021.03.034
76. He J, Gao Y, Yang C, Guo Y, Liu L, Lu S, He H. Navigating the landscape: Prospects and hurdles in targeting vascular smooth muscle cells for atherosclerosis diagnosis and therapy. *J Control Release*. 2024;366:261-281. doi: 10.1016/j.jconrel.2023.12.047
77. Ruchoux MM, Domenga V, Brulin P, Maciazek J, Limol S, Tournier-Lasserve E, Joutel A. Transgenic mice expressing mutant Notch3 develop vascular alterations characteristic of cerebral autosomal dominant arteriopathy with subcortical infarcts and leukoencephalopathy. *Am J Pathol*. 2003;162:329-342. doi: 10.1016/S0002-9440(10)63824-2
78. Chastney MR, Kaivola J, Leppanen VM, Ivaska J. The role and regulation of integrins in cell migration and invasion. *Nat Rev Mol Cell Biol*. 2025;26:147-167. doi: 10.1038/s41580-024-00777-1
79. Tapial Martinez P, Lopez Navajas P, Lietha D. FAK Structure and Regulation by Membrane Interactions and Force in Focal Adhesions. *Biomolecules*. 2020;10. doi: 10.3390/biom10020179
80. Frismantiene A, Philippova M, Erne P, Resink TJ. Smooth muscle cell-driven vascular diseases and molecular mechanisms of VSMC plasticity. *Cell Signal*. 2018;52:48-64. doi: 10.1016/j.cellsig.2018.08.019
81. Frisch SM, Vuori K, Ruoslahti E, Chan-Hui PY. Control of adhesion-dependent cell survival by focal adhesion kinase. *J Cell Biol*. 1996;134:793-799. doi: 10.1083/jcb.134.3.793
82. McLean GW, Carragher NO, Avizienyte E, Evans J, Brunton VG, Frame MC. The role of focal-adhesion kinase in cancer - a new therapeutic opportunity. *Nat Rev Cancer*. 2005;5:505-515. doi: 10.1038/nrc1647
83. Haun F, Neumann S, Peintner L, Wieland K, Habicht J, Schwan C, Ostevold K, Koczorowska MM, Biniossek M, Kist M, et al. Identification of a novel anoikis signalling pathway using the fungal virulence factor gliotoxin. *Nat Commun*. 2018;9:3524. doi: 10.1038/s41467-018-05850-w
84. Buchwalow IB, Cacanyiova S, Neumann J, Samoilova VE, Boecker W, Kristek F. The role of arterial smooth muscle in vasorelaxation. *Biochem Biophys Res Commun*. 2008;377:504-507. doi: 10.1016/j.bbrc.2008.10.019
85. Buchwalow IB, Podzuweit T, Bocker W, Samoilova VE, Thomas S, Wellner M, Baba HA, Robenek H, Schnekenburger J, Lerch MM. Vascular smooth muscle and nitric oxide synthase. *FASEB J*. 2002;16:500-508. doi: 10.1096/fj.01-0842com
86. Kang TM. Unconventional eNOS in pulmonary artery smooth muscles: why should it be there? *Pflugers Arch*. 2019;471:1245-1246. doi: 10.1007/s00424-019-02308-w
87. Chang AC, Fu Y, Garside VC, Niessen K, Chang L, Fuller M, Setiadi A, Smrz J, Kyle A, Minchinton A, et al. Notch initiates the endothelial-to-mesenchymal transition in the atrioventricular canal through autocrine activation of soluble guanylyl cyclase. *Dev Cell*. 2011;21:288-300. doi: 10.1016/j.devcel.2011.06.022
88. Neves KB, Morris HE, Alves-Lopes R, Muir KW, Moreton F, Delles C, Montezano AC, Touyz RM. Peripheral arteriopathy caused by Notch3 gain-of-function mutation

involves ER and oxidative stress and blunting of NO/sGC/cGMP pathway. *Clin Sci (Lond)*. 2021;135:753-773. doi: 10.1042/CS20201412
89. Bonetti J, Corti A, Lerouge L, Pompella A, Gaucher C. Phenotypic Modulation of Macrophages and Vascular Smooth Muscle Cells in Atherosclerosis-Nitro-Redox Interconnections. *Antioxidants (Basel)*. 2021;10. doi: 10.3390/antiox10040516
90. Babaei S, Stewart DJ. Overexpression of endothelial NO synthase induces angiogenesis in a co-culture model. *Cardiovasc Res*. 2002;55:190-200. doi: 10.1016/s0008-6363(02)00287-0
91. Koneru S, Varma Penumathsa S, Thirunavukkarasu M, Vidavalur R, Zhan L, Singal PK, Engelman RM, Das DK, Maulik N. Sildenafil-mediated neovascularization and protection against myocardial ischaemia reperfusion injury in rats: role of VEGF/angiopoietin-1. *J Cell Mol Med*. 2008;12:2651-2664. doi: 10.1111/j.1582-4934.2008.00319.x
92. Sahara M, Sata M, Morita T, Nakajima T, Hirata Y, Nagai R. A phosphodiesterase-5 inhibitor vardenafil enhances angiogenesis through a protein kinase G-dependent hypoxia-inducible factor-1/vascular endothelial growth factor pathway. *Arterioscler Thromb Vasc Biol*. 2010;30:1315-1324. doi: 10.1161/ATVBAHA.109.201327
93. Choi HI, Kang BM, Jang J, Hwang ST, Kwon O. Novel effect of sildenafil on hair growth. *Biochem Biophys Res Commun*. 2018;505:685-691. doi: 10.1016/j.bbrc.2018.09.164
94. Fang J, Zhang P, Zhou Y, Chiang CW, Tan J, Hou Y, Stauffer S, Li L, Pieper AA, Cummings J, et al. Endophenotype-based in silico network medicine discovery combined with insurance record data mining identifies sildenafil as a candidate drug for Alzheimer's disease. *Nat Aging*. 2021;1:1175-1188. doi: 10.1038/s43587-021-00138-z
95. Acquarone E, Argyrousi EK, van den Berg M, Gulisano W, Fa M, Staniszewski A, Calcagno E, Zuccarello E, D'Adamio L, Deng SX, et al. Synaptic and memory dysfunction induced by tau oligomers is rescued by up-regulation of the nitric oxide cascade. *Mol Neurodegener*. 2019;14:26. doi: 10.1186/s13024-019-0326-4
96. Zuccarello E, Acquarone E, Calcagno E, Argyrousi EK, Deng SX, Landry DW, Arancio O, Fiorito J. Development of novel phosphodiesterase 5 inhibitors for the therapy of Alzheimer's disease. *Biochem Pharmacol*. 2020;176:113818. doi: 10.1016/j.bcp.2020.113818
97. Wadman M. FDA no longer has to require animal testing for new drugs. *Science*. 2023;379:127-128. doi: 10.1126/science.adg6276
98. Carratt SA, Zuch de Zafra CL, Oziolor E, Rana P, Vansell NR, Mangipudy R, Vaidya VS. An industry perspective on the FDA Modernization Act 2.0/3.0: potential next steps for sponsors to reduce animal use in drug development. *Toxicol Sci*. 2025;203:28-34. doi: 10.1093/toxsci/kfae122
99. Cheung C, Bernardo AS, Pedersen RA, Sinha S. Directed differentiation of embryonic origin-specific vascular smooth muscle subtypes from human pluripotent stem cells. *Nat Protoc*. 2014;9:929-938. doi: 10.1038/nprot.2014.059
100. Maranga JO, Justine John Nnko, and Shengwu Xiong. Learned active contours via transformer-based deep convolutional neural network using canny edge detection algorithm. *Signal, Image and Video Processing* 2025;19.3:222.
101. Hosang J, Rodrigo Benenson, and Bernt Schiele. Learning non-maximum suppression. *Proceedings of the IEEE conference on computer vision and pattern recognition*. 2017.
102. Kanopoulos N, Nagesh Vasanthavada, and Robert L. Design of an image edge detection filter using the Sobel operator. *IEEE Journal of solid-state circuits* 1988;23.2:358-367.

## Acknowledgement

The study is partially supported by the British Heart Foundation (PG/12/31/2952). We thank Dr Adam Dickinson for his contribution to the establishment of the iPSC lines. We thank Dr. Helen Murphy and Iris Trender-Gerhard from Manchester Centre for Genomic Medicine for help in recruiting and taking biopsies from CADASIL patients, and Meenakshi Minnis and Stephen Trueman of MCGM for help in growing HDFs and karyotyping iPSCs. We would like to thank Prof Richard Bains for his PhD supervising role and valuable suggestions. We would like to thank the University of Manchester Bioimaging Core Facility for guidance on confocal microscopy and sample preparation. We wish to thank Dr Aleksandr Mironov in the FBMH EM Core Facility (RRID:SCR_021147) for his assistance and the Wellcome Trust for equipment grant support to the EM Facility. The authors would like to thank Rachel Scholey and Andy Hayes of the Bioinformatics and Genomic Technologies Core Facilities at the University of Manchester for providing support regarding RNAseq. We thank Prof Susan J Kimber's group for sharing their colony isolating facilities. We are grateful to Shi-yang Li for his assistance with the RNAseq analysis using R code. CY is supported by a Post-Doctoral Fellowship from the China Scholarship Council (ref No.201908500055).

## Author contributions

T.W. conceptualised and designed study, supervised the project, and manuscript writing. X.Z. performed most experiments and conducted data acquisition and analysis; contributed to manuscript writing. C.Y. and A.A: contributed to the generation of isogenic controls using CRISPR/Cas9. A.Z and H.Z: Developed AI tools for imaging analysis. P.S. Contributed to CADASIL patient recruitment and skin biopsy and manuscript proofreading.

## Competing interests

The authors declare no competing interests.

## Figure legends

**Figure 1. Lineage-specific VSMC differentiation from iPSCs**. **a** Diagram illustrating protocols used for differentiating iPSCs into VSMCs via neural crest lineage (NC-SMCs), lateral plate mesoderm lineage (LPM-SMCs) and paraxial mesoderm lineage (PM-SMCs). **b** RT-qPCR determination of marker gene expressions showing downregulation of pluripotency marker gene *OCT4* during VSMC differentiation, upregulation of the lineage-specific maker genes, *TFAP2A*, *ISL1* and *TBX6,* at the respective progenitor stages, and increased expression of VSMC marker gene *MYH11* in differentiated VSMCs. **c** IPSC-derived lineage-specific VSMCs on differentiation day 18 were immunofluorescent stained with VSMC markers, α-SMA (green) and calponin (red), and nuclear counterstained by DAPI (blue). **d** Proliferation of lineage-specific VSMCs was determined by ki67 immunofluorescent staining. **e** Migration of lineage-specific VSMCs was determined by IncuCyte live cell imaging of wound healing assay. **f** Contraction of lineage-specific VSMCs was determined by collagen I gel contraction assay and quantified (right panel). **g** Vinculin immunofluorescent staining (red) of iPSC derived VSMCs showing focal adhesions and its quantitation (right panel). F-actin was stained green.

Scale bars,100μm in **c** and **g**. Data are presented as mean ± SEM from at least 3 independent iPSC differentiations (n=3). One-way ANOVA and Tukey's post hoc test in **b**, **d**, **f** and **g,** or two-way ANOVA before post hoc test demonstrating overall differences between groups in **e**, *p ≤ 0.05, **p ≤ 0.01, ***p ≤ 0.001, ****p ≤ 0.0001.

**Figure 2. Comparison of behaviours and functions between lineage-specific VSMCs derived from CADASIL iPSCs.** IPSCs from two CADASIL patients (R153C & C224Y) and their isogenic controls (isoCtrl) were differentiated into lineage-specific VSMCs: NC-SMCs, LPM-SMCs and PM-SMCs, respectively. **a** Cell proliferation was determined by immunofluorescent staining of Ki67 (red). Nuclei were counter stained by DAPI (blue). Results were quantified and showed in the lower panel. Scale bars = 100 μm. **b** Cell migration was determined by IncuCyte live cell imaging of wound healing assay. **c** Cell contraction was determined by collagen I contraction assay which was quantified (right panel). **d** Focal adhesion was visualised by vinculin immunofluorescent staining (red) which was quantified (right panel). F-actin was stained green. Scale bars = 100 μm in **a** and **d**. All quantifiable data are presented as mean ± SEM from 3 independent iPSC differentiations (n=3). Unpaired Student's *t* test in **a**, **c** and **d**. Two-way ANOVA before post-hoc test demonstrating overall differences between groups in **b**, *p ≤ 0.05, **p ≤ 0.01, ****p ≤ 0.0001.

**Figure 3. Analyses of RNA sequencing data.** IPSCs from two CADASIL patients (R135C & C224Y) and respective isogenic controls (isoCtrl) as well as three wild-type iPSC control lines (WT1-3) were differentiated into iVSMCs via neural crest lineage (NC) which were subjected to RNA sequencing. **a** Principal component (PCA) plot. **b** Heatmap showing differentially expressed genes (DEGs) between iVSMCs of the two patients and five controls (2x isoCtrls and 3x WT controls). **c** Volcano plot comparing DEGs between CADASIL patients (R135C & C224Y) and their isogenic controls (R153C_isoCtrl and C224Y_isoCtrl). **d** GO (gene ontology) term enrichment analysis of DEGs from the RNAseq data. BP, biological processes, CC, cellular components, MF, molecular functions.

**Figure 4. Phenotype switching of iPSC derived CADASIL iVSMCs.** IPSCs from two CADASIL patients (R135C & C224Y) and their isogenic controls (R153C_isoCtrl and C224Y_isoCtrl) were differentiated into iVSMCs via neural crest (NC). **a** Diagram illustrating principles of VSMC switching from a contractile to a synthetic phenotype and associated key marker gene expressions. **b** Heatmap showing differentially expressed VSMC contractile and synthetic marker genes from RNA sequencing (RNAseq) results of the two CADASIL and their isogenic control iVSMCs. **c** RT-qPCR confirmation of the up- and down-regulations of major VSMC contractile and synthetic marker genes in CADASIL iVSMCs. Data are presented as mean ± SEM from 3 independent iPSC differentiations (n=3). Fold change of gene expressions for each gene were calculated separately and compared by unpaired Student's *t* test. **d** Western blotting (WB) confirmation of downregulations of key VSMC contractile proteins, α-SMA, calponin, SM22α and MLCK, in CADASIL iVSMCs, comparing to their isogenic controls. Quantifications of the WB results show in the panel below. Data are presented as mean ± SEM from 3 independent iPSC differentiations with 3 technical replicants in each experiment (n=3). Unpaired Student's *t* test, *p ≤ 0.05, **p ≤ 0.01. **e** Chord diagram generated showing relationship between some of the VSMC phenotype related Gene Ontology (GO) terms and differentially expressed genes (DEGs). Diagram **a** was Created with BioRender.com.

**Figure 5. Extracellular matrix (ECM) accumulation in CADASIL iVSMCs.** IPSCs from two CADASIL patients (R135C & C224Y) and their isogenic controls (R153C_isoCtrl and C224Y_isoCtrl) were differentiated into iVSMCs via neural crest (NC) lineage. **a** Gene set enrichment analysis (GSEA) plot of RNA sequencing data on gene ontology (GO) categories of ECM structural constituent, collagen biosynthesis and modifying enzymes, and collagen trimer in CADASIL iVSMCs versus their isogenic controls. **b** RT-qPCR confirmation of differentially expressed major extracellular matrix genes in CADASIL iVSMCs versus isogenic controls. Data are presented as mean ± SEM from 3 independent iPSC differentiations (n=3). Fold changes of gene expression for each gene were calculated separately and compared by unpaired Student's *t* test. **c** Collagen IV immunofluorescent staining of iVSMCs spheroids derived from iPSCs of CADASIL and isoCtrls. Nuclei were counterstained by DAPI. Scale bar = 50μm. **d** TEM images of iVSMCs derived from iPSCs of CADASIL and isoCtrls. White arrows, smooth cell membranes between adjacent cells. Red asterisk star, vanish of cell junctions and accumulation of extracellular materials in CADASIL iVSMCs. Yellow asterisk star, ECM accumulation. **e** Notch3 extracellular domain (N3ECD) immunofluorescent staining of iVSMCs spheroids derived from iPSCs of CADASIL and isoCtrls. Nuclei were counterstained by DAPI. Scale bar = 50μm. **f** Western blotting (WB) of iVSMCs using antibodies against N3ECD or Notch3 intracellular domain (N3ICD). Quantifications of the WB results are shown in the lower panel. Data are presented as mean ± SEM from 3 independent iPSC differentiations (n=3). Unpaired Student's *t* test, **p ≤ 0.01.

**Figure 6. Disruption of cell-matrix and cell-cell interaction of CADASIL iVSMCs leading to cell death. a** KEGG pathway enrichment of differentially expressed genes (DEGs) between iVSMCs of CADASIL patients and isogenic controls on the RNA sequencing data. **b** A schematic diagram illustrating main components of focal adhesion complex. **c** RT-qPCR determination of the expression of integrin subtypes in iVSMCs derived from iPSCs of CADASIL and their isogenic controls (isoCtrls). Data are presented as mean ± SEM (n=3). Fold changes of gene expression for each gene were calculated separately and compared by unpaired Student's *t* test. **d** Western blotting of (WB) FAK and p-FAK in iVSMCs derived from iPSCs of CADASIL and isoCtrl. Quantifications of the WB results are shown in the lower panel. Data are presented as mean ± SEM (n=3). Unpaired Student's *t* test, *p ≤ 0.05, **p ≤ 0.01, ***p ≤ 0.001. **e** F-actin staining of iVSMCs derived from iPSCs of CADASIL and isoCtrls. Nuclei were counterstained by DAPI. Scale bar = 5μm.**f** Organisations of actin cytoskeletons in **e** were analysed by an artificial intelligent (AI) assisted algorithm and presented as special dispersion of actin filament, which was quantified. Unpaired Student's *t* test, ****p ≤ 0.0001. **g** Gene set enrichment analysis (GSEA) plot of RNA sequencing data on gene Ontology (GO) categories of ECM-receptor interaction and adherens junction in CADASIL iVSMCs versus isoCtrls. **h** Live/dead staining of iVSMCs derived from iPSCs of CADASIL and isoCtrls using Calcein-AM (Cal-AM) and BOBO-3 iodide (BOBO-3), respectively. Scale bar = 100 μm. **i** Quantification of the live/dead staining result in **h**. Data are mean ± SEM (n=3). Unpaired Student's *t* test, ***p ≤ 0.001, ****p ≤ 0.0001. Results in **c**, **d**, **e** and **h** were all from at least 3 independent iPSC differentiations. Diagram **b** was Created with BioRender.com.

**Figure 7. Nitric oxide signalling from iPSC derived VSMCs.** IPSCs from two CADASIL patients (R135C & C224Y) and their isogenic controls (R153C_isoCtrl and C224Y_isoCtrl) were differentiated into iVSMCs via neural crest (NC) lineage. **a** Diagram illustrating NO-sGC-cGMP-PKG signalling pathway. **b** & **c** Determination of *GUCY1A1* and *GUCY1B1* expressions by RT-qPCR (**b**) and their protein levels (GCSα1 and GCSβ1) by western blotting (**c**) in iVSMCs derived from CADASIL and isogenic control (isoCtrl) iPSC lines. **d** Cellular nitric oxide

(NO) levels in iVSMCs determined by DAF-AM staining and their quantifications (right panel). Scale bar = 100μm. **e** Expressions of *PRKG* and *VASP* in iVSMCs determined by RT-qPCR in iVSMCs. **f** & **g** Western blotting determination of protein levels of VASP (**f**) and AKT and p-AKT (**g**) in iVSMCs. **h** Immunofluorescent staining of eNOS in iVSMCs. Scale bar = 5μm. All quantitative data are presented as mean ± SEM from 3 independent iPSC differentiations (n=3). Unpaired Student's *t* test, *p ≤ 0.05, **p ≤ 0.01, and ***p ≤ 0.001. Diagram **a** was Created with BioRender.com.

**Figure 8. SNAP and Sildenafil rescue of abnormal proliferation, contraction and cell death of CADASIL iVSMCs.** IPSCs from two CADASIL patients (R135C & C224Y) and their isogenic controls (R153C_isoCtrl and C224Y_isoCtrl) were differentiated into iVSMCs via neural crest (NC) lineage. The cells were subjected to proliferation assay by Ki67 immunofluorescent staining (**a**) in the presence or absence of the nitric oxide (NO) donor (SNAP) or PDE5 inhibitor (Sildenafil), and results were quantified (**b** & **c**). Scale bars = 100 μm. **d** & **e** Western blotting determination of protein levels of αSMA and GCSα1 with or without SNAP treatment (**d**), αSMA with or without Sildenafil treatment (**e**), and calponin and MLCK with or without SNAP or Sildenafil treatment, respectively, in iVSMCs. Results were quantified and normalised to the total protein loading control (representative areas are shown under each blot). **f** F-actin staining of iVSMCs derived from iPSCs of CADASIL and isoCtrls treated with or without SNAP or Sildenafil. Nuclei were counterstained by DAPI. The organisations of actin cytoskeletons were analysed and quantified by an artificial intelligent (AI) assisted algorithm and presented as special dispersion of actin filament showing in the lower panel. Scale bars = 5 μm. **g** Live/dead staining of iVSMCs derived from iPSCs of CADASIL and isoCtrls using Calcein-AM (Cal-AM) and BOBO-3 iodide (BOBO-3), respectively. Data were quantified shown in the lower panel. Scale bars = 100 μm. All quantitative data are presented as mean ± SEM from 3 independent iPSC differentiations (n=3). Two-way ANOVA and Tukey's post hoc test, *p ≤ 0.05, **p ≤ 0.01, ***p ≤ 0.001, and ****p ≤ 0.0001.

**Figure 9. SNAP and Sildenafil rescue of impaired CADASIL iVSMCs in supporting angiogenesis.** IPSCs from two CADASIL patients (R135C & C224Y) and their isogenic controls (R153C_isoCtrl and C224Y_isoCtrl) were differentiated into iVSMCs via neural crest lineage. *In vitro* angiogenesis with combined HUVECs and iVSMCs was carried out on Matrigel in the presence or absence of nitric oxide (NO) donor (SNAP) or PDE5 inhibitor (Sildenafil). Quantification of the angiogenesis results showing on the fitted smooth trend lines (LOESS/liner) with 95% confidence interval showing that both SNAP and Sildenafil significantly reversed the impaired ability of CADASIL iVSMCs in supporting the stability of the angiogenic tubule structures. Data are presented as mean ± SEM from 3 independent iPSC differentiations (n=3). Two-way ANOVA and Tukey's post hoc test were conducted. Asterisk stars (*s) showing significant differences of the treated versus non-treated samples of CADASIL iVSMCs at the indicated time points. *p ≤ 0.05, **p ≤ 0.01, and ***p ≤ 0.001.

**Figure 1.**

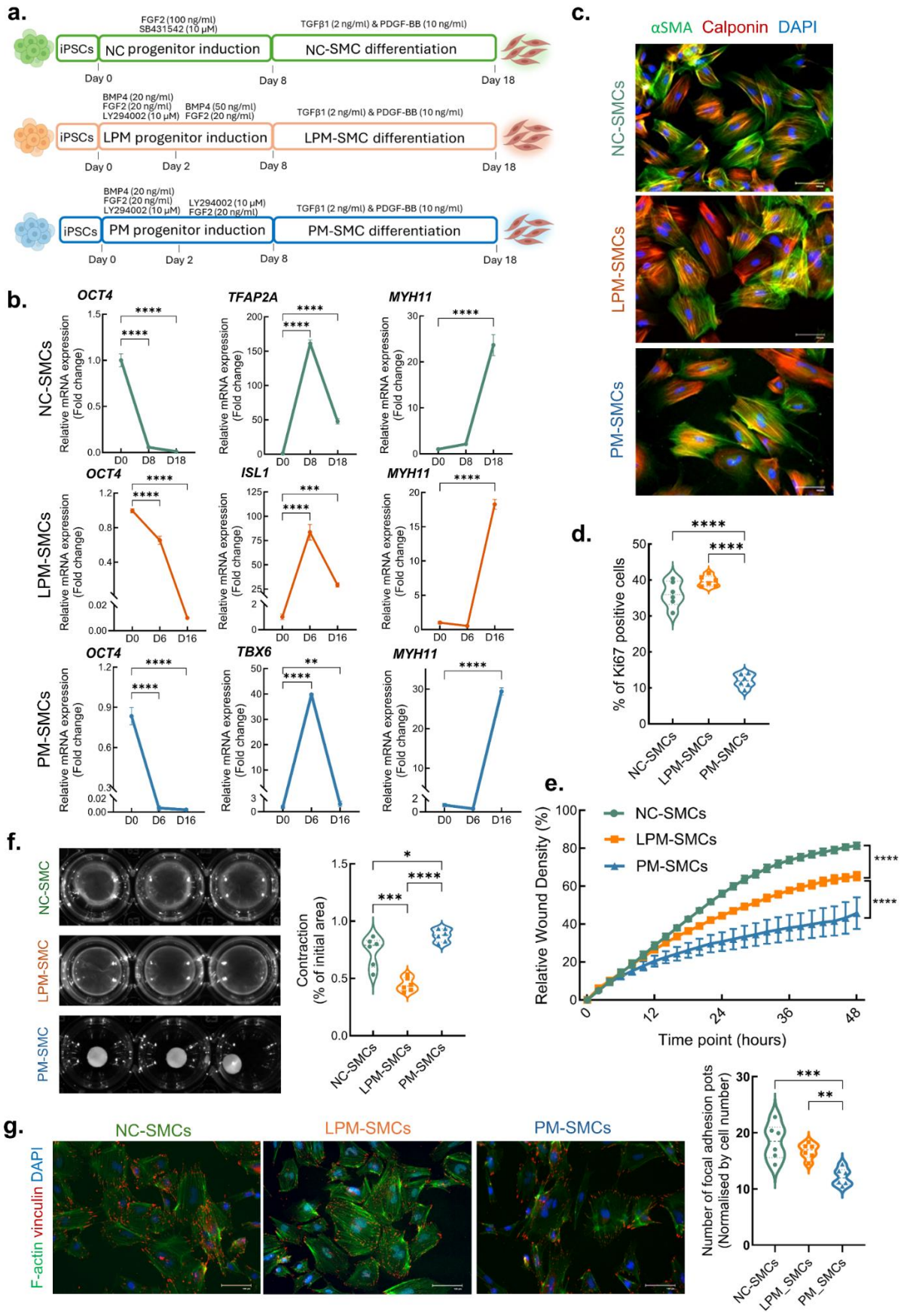
a.
FGF2 (100 ng/ml)
SB431542 (10 μM)
TGFβ1 (2 ng/ml) & PDGF-BB (10 ng/ml)
iPSCs
NC progenitor induction
NC-SMC differentiation
Day 0
Day 8
Day 18
BMP4 (20 ng/ml)
FGF2 (20 ng/ml)
LY294002 (10 μM)
BMP4 (50 ng/ml)
FGF2 (20 ng/ml)
TGFβ1 (2 ng/ml) & PDGF-BB (10 ng/ml)
iPSCs
LPM progenitor induction
LPM-SMC differentiation
Day 0
Day 2
Day 8
Day 18
BMP4 (20 ng/ml)
FGF2 (20 ng/ml)
LY294002 (10 μM)
LY294002 (10 μM)
FGF2 (20 ng/ml)
TGFβ1 (2 ng/ml) & PDGF-BB (10 ng/ml)
iPSCs
PM progenitor induction
PM-SMC differentiation
Day 0
Day 2
Day 8
Day 18
b.
NC-SMCs
LPM-SMCs
PM-SMCs
OCT4
TFAP2A
MYH11
ISL1
TBX6
Relative mRNA expression (Fold change)
D0
D8
D18
D6
D16
c.
αSMA Calponin DAPI
NC-SMCs
LPM-SMCs
PM-SMCs
d.
% of Ki67 positive cells
NC-SMCs
LPM-SMCs
PM-SMCs
e.
NC-SMCs
LPM-SMCs
PM-SMCs
Relative Wound Density (%)
Time point (hours)
f.
NC-SMC
LPM-SMC
PM-SMC
Contraction (% of initial area)
NC-SMCs
LPM-SMCs
PM-SMCs
g.
NC-SMCs
LPM-SMCs
PM-SMCs
F-actin vinculin DAPI
Number of focal adhesion pots (Normalised by cell number)
NC-SMCs
LPM_SMCs
PM_SMCs

**Figure 2.**

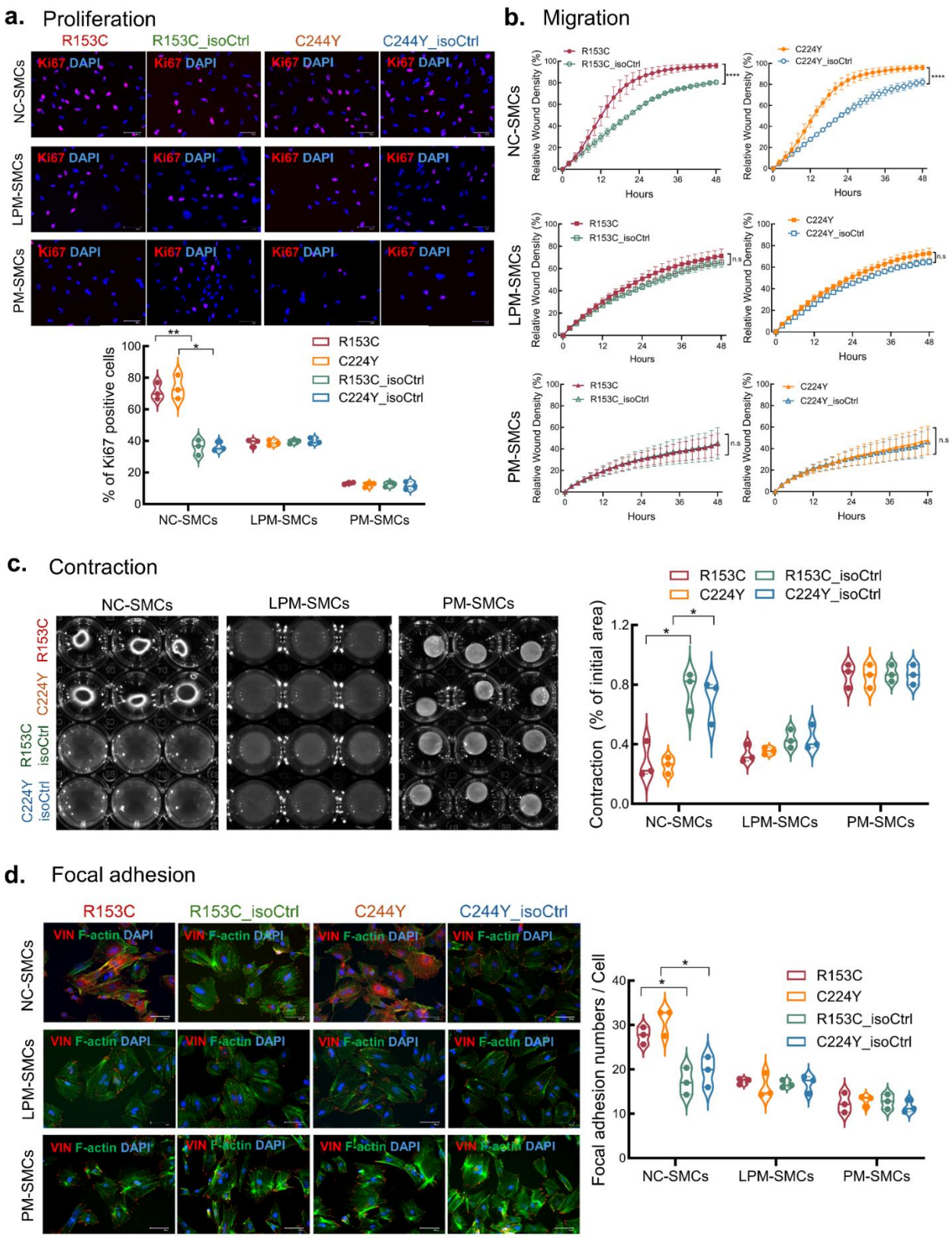
a. Proliferation
R153C
R153C_isoCtrl
C244Y
C244Y_isoCtrl
NC-SMCs
LPM-SMCs
PM-SMCs
Ki67 DAPI
% of Ki67 positive cells
R153C
C224Y
R153C_isoCtrl
C224Y_isoCtrl
b. Migration
Relative Wound Density (%)
Hours
c. Contraction
NC-SMCs
LPM-SMCs
PM-SMCs
Contraction (% of initial area)
d. Focal adhesion
VIN F-actin DAPI
Focal adhesion numbers / Cell

**Figure 3.**

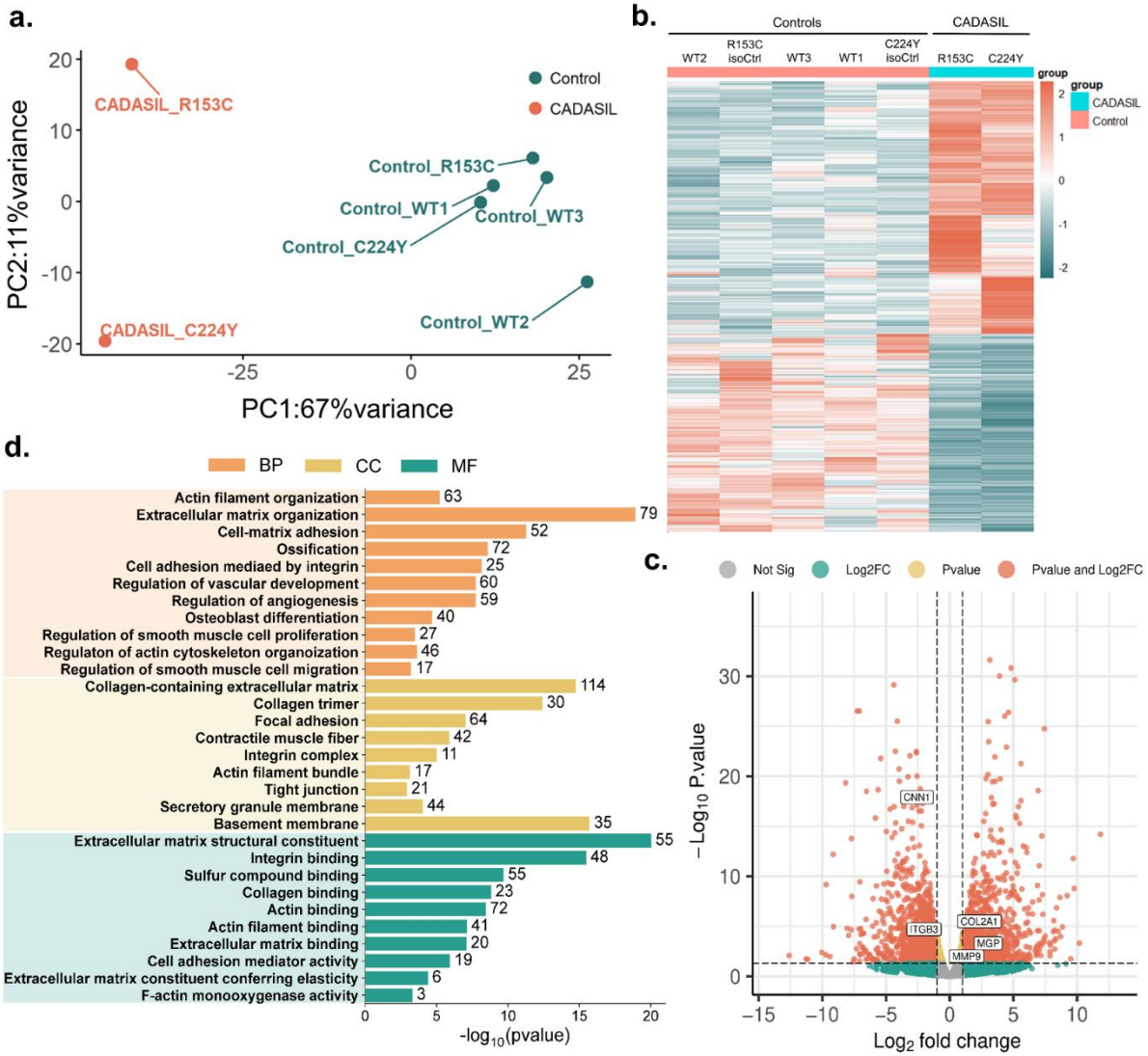
a.
PC2:11%variance
PC1:67%variance
Control
CADASIL
CADASIL_R153C
CADASIL_C224Y
Control_R153C
Control_WT1
Control_WT3
Control_C224Y
Control_WT2
b.
Controls
CADASIL
WT2
R153C isoCtrl
WT3
WT1
C224Y isoCtrl
R153C
C224Y
group
CADASIL
Control
c.
Not Sig
Log2FC
Pvalue
Pvalue and Log2FC
−Log10 P.value
Log2 fold change
CNN1
ITGB3
COL2A1
MGP
MMP9
d.
BP
CC
MF
Actin filament organization 63
Extracellular matrix organization 79
Cell-matrix adhesion 52
Ossification 72
Cell adhesion mediaed by integrin 25
Regulation of vascular development 60
Regulation of angiogenesis 59
Osteoblast differentiation 40
Regulation of smooth muscle cell proliferation 27
Regulaton of actin cytoskeleton organoization 46
Regulation of smooth muscle cell migration 17
Collagen-containing extracellular matrix 114
Collagen trimer 30
Focal adhesion 64
Contractile muscle fiber 42
Integrin complex 11
Actin filament bundle 17
Tight junction 21
Secretory granule membrane 44
Basement membrane 35
Extracellular matrix structural constituent 55
Integrin binding 48
Sulfur compound binding 55
Collagen binding 23
Actin binding 72
Actin filament binding 41
Extracellular matrix binding 20
Cell adhesion mediator activity 19
Extracellular matrix constituent conferring elasticity 6
F-actin monooxygenase activity 3
-log10(pvalue)

**Figure 4.**

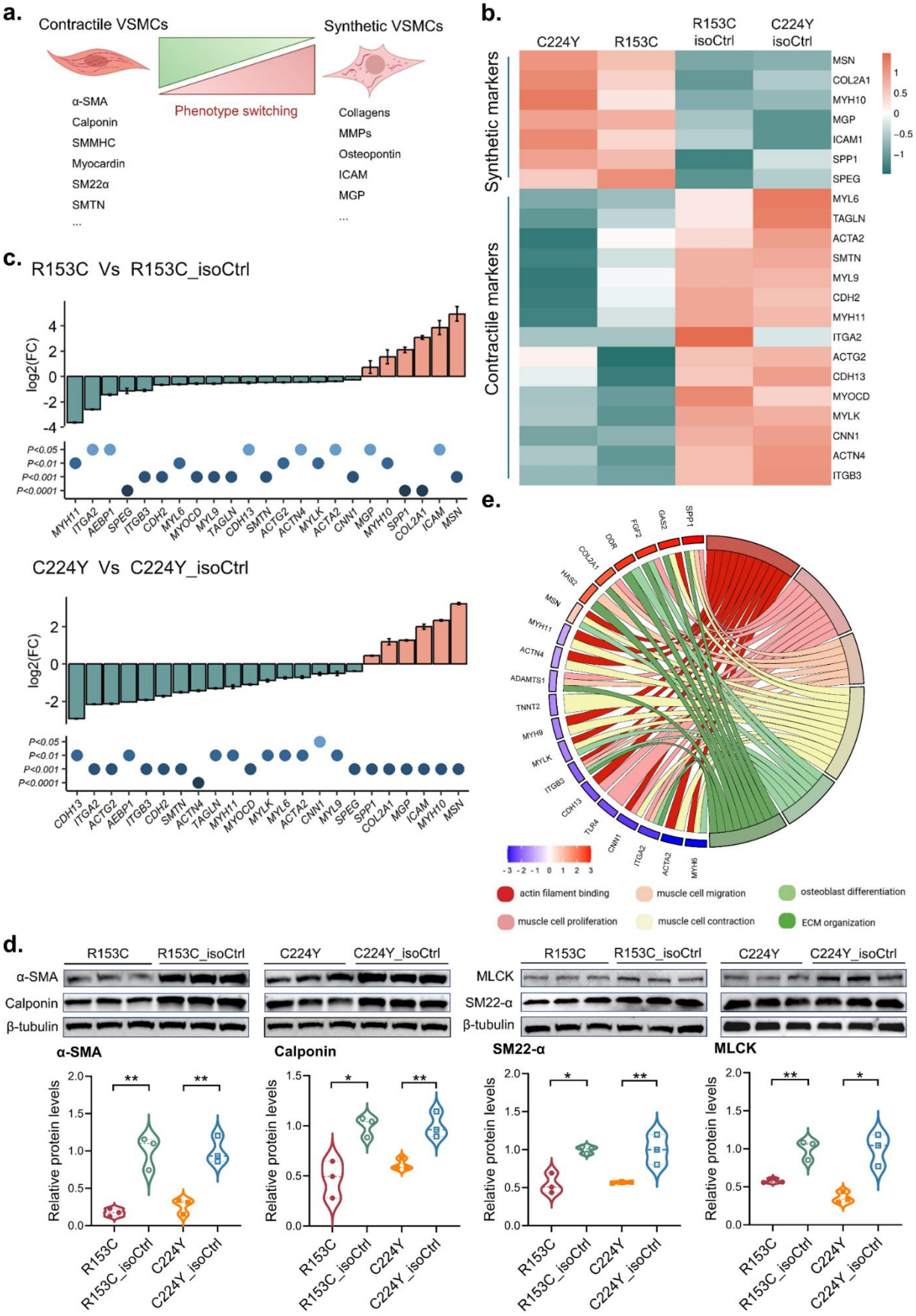
a.
Contractile VSMCs
Synthetic VSMCs
Phenotype switching
α-SMA
Calponin
SMMHC
Myocardin
SM22α
SMTN
...
Collagens
MMPs
Osteopontin
ICAM
MGP
...
b.
C224Y
R153C
R153C isoCtrl
C224Y isoCtrl
Synthetic markers
Contractile markers
MSN
COL2A1
MYH10
MGP
ICAM1
SPP1
SPEG
MYL6
TAGLN
ACTA2
SMTN
MYL9
CDH2
MYH11
ITGA2
ACTG2
CDH13
MYOCD
MYLK
CNN1
ACTN4
ITGB3
c.
R153C Vs R153C_isoCtrl
log2(FC)
P<0.05
P<0.01
P<0.001
P<0.0001
MYH11 ITGA2 AEBP1 SPEG ITGB3 CDH2 MYL6 MYOCD MYL9 TAGLN CDH13 SMTN ACTG2 ACTN4 MYLK ACTA2 CNN1 MGP MYH10 SPP1 COL2A1 ICAM MSN
C224Y Vs C224Y_isoCtrl
CDH13 ITGA2 ACTG2 AEBP1 ITGB3 CDH2 SMTN ACTN4 TAGLN MYH11 MYOCD MYLK MYL6 ACTA2 CNN1 MYL9 SPEG SPP1 COL2A1 MGP ICAM MYH10 MSN
e.
actin filament binding
muscle cell migration
osteoblast differentiation
muscle cell proliferation
muscle cell contraction
ECM organization
d.
R153C
R153C_isoCtrl
C224Y
C224Y_isoCtrl
α-SMA
Calponin
β-tubulin
MLCK
SM22-α
Relative protein levels

**Figure 5.**

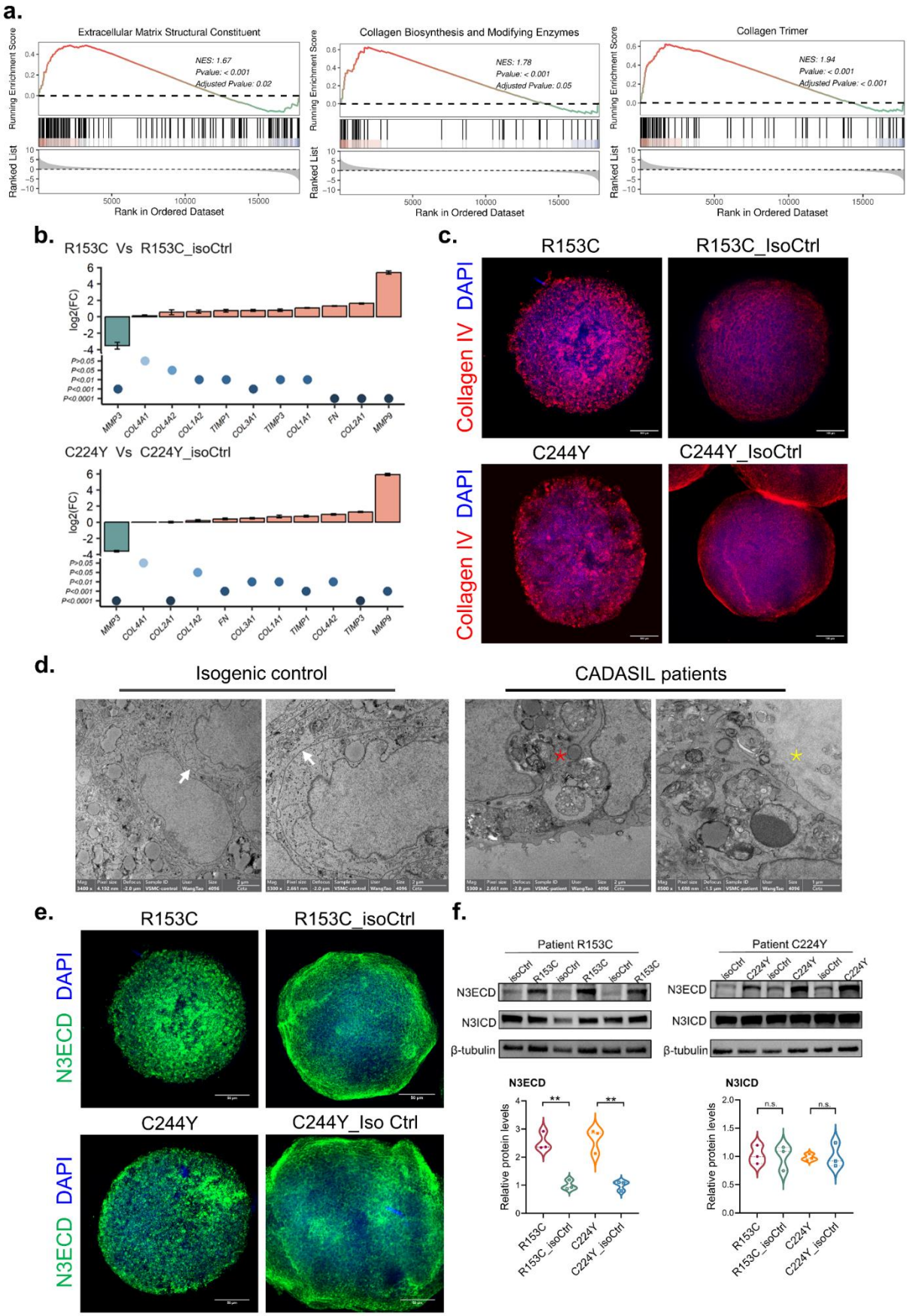
a.
Extracellular Matrix Structural Constituent
NES: 1.67
Pvalue: < 0.001
Adjusted Pvalue: 0.02
Collagen Biosynthesis and Modifying Enzymes
NES: 1.78
Pvalue: < 0.001
Adjusted Pvalue: 0.05
Collagen Trimer
NES: 1.94
Pvalue: < 0.001
Adjusted Pvalue: < 0.001
Running Enrichment Score
Ranked List
Rank in Ordered Dataset
b.
R153C Vs R153C_isoCtrl
log2(FC)
MMP3
COL4A1
COL4A2
COL1A2
TIMP1
COL3A1
TIMP3
COL1A1
FN
COL2A1
MMP9
C224Y Vs C224Y_isoCtrl
c.
R153C
R153C_IsoCtrl
C244Y
C244Y_IsoCtrl
Collagen IV DAPI
d.
Isogenic control
CADASIL patients
e.
R153C
R153C_isoCtrl
C244Y
C244Y_Iso Ctrl
N3ECD DAPI
f.
Patient R153C
Patient C224Y
N3ECD
N3ICD
β-tubulin
Relative protein levels
n.s.

**Figure 6.**

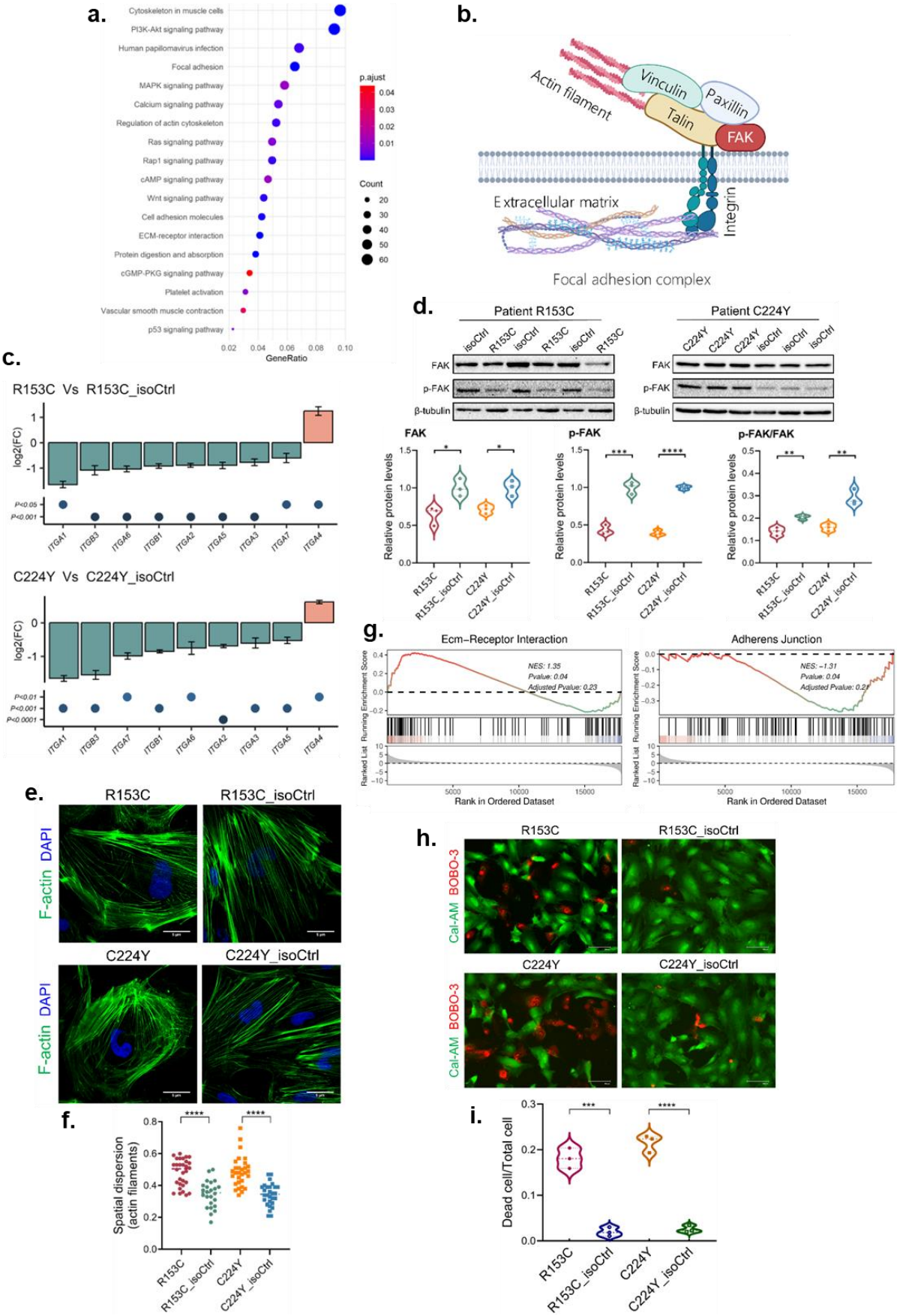
a.
Cytoskeleton in muscle cells
PI3K-Akt signaling pathway
Human papillomavirus infection
Focal adhesion
MAPK signaling pathway
Calcium signaling pathway
Regulation of actin cytoskeleton
Ras signaling pathway
Rap1 signaling pathway
cAMP signaling pathway
Wnt signaling pathway
Cell adhesion molecules
ECM-receptor interaction
Protein digestion and absorption
cGMP-PKG signaling pathway
Platelet activation
Vascular smooth muscle contraction
p53 signaling pathway
GeneRatio
p.ajust
Count
b.
Actin filament
Vinculin
Paxillin
Talin
FAK
Extracellular matrix
Integrin
Focal adhesion complex
c.
R153C Vs R153C_isoCtrl
log2(FC)
C224Y Vs C224Y_isoCtrl
d.
Patient R153C
Patient C224Y
FAK
p-FAK
β-tubulin
Relative protein levels
p-FAK/FAK
g.
Ecm−Receptor Interaction
Adherens Junction
Rank in Ordered Dataset
e.
R153C
R153C_isoCtrl
C224Y
C224Y_isoCtrl
F-actin DAPI
f.
Spatial dispersion (actin filaments)
h.
Cal-AM BOBO-3
i.
Dead cell/Total cell

**Figure 7.**

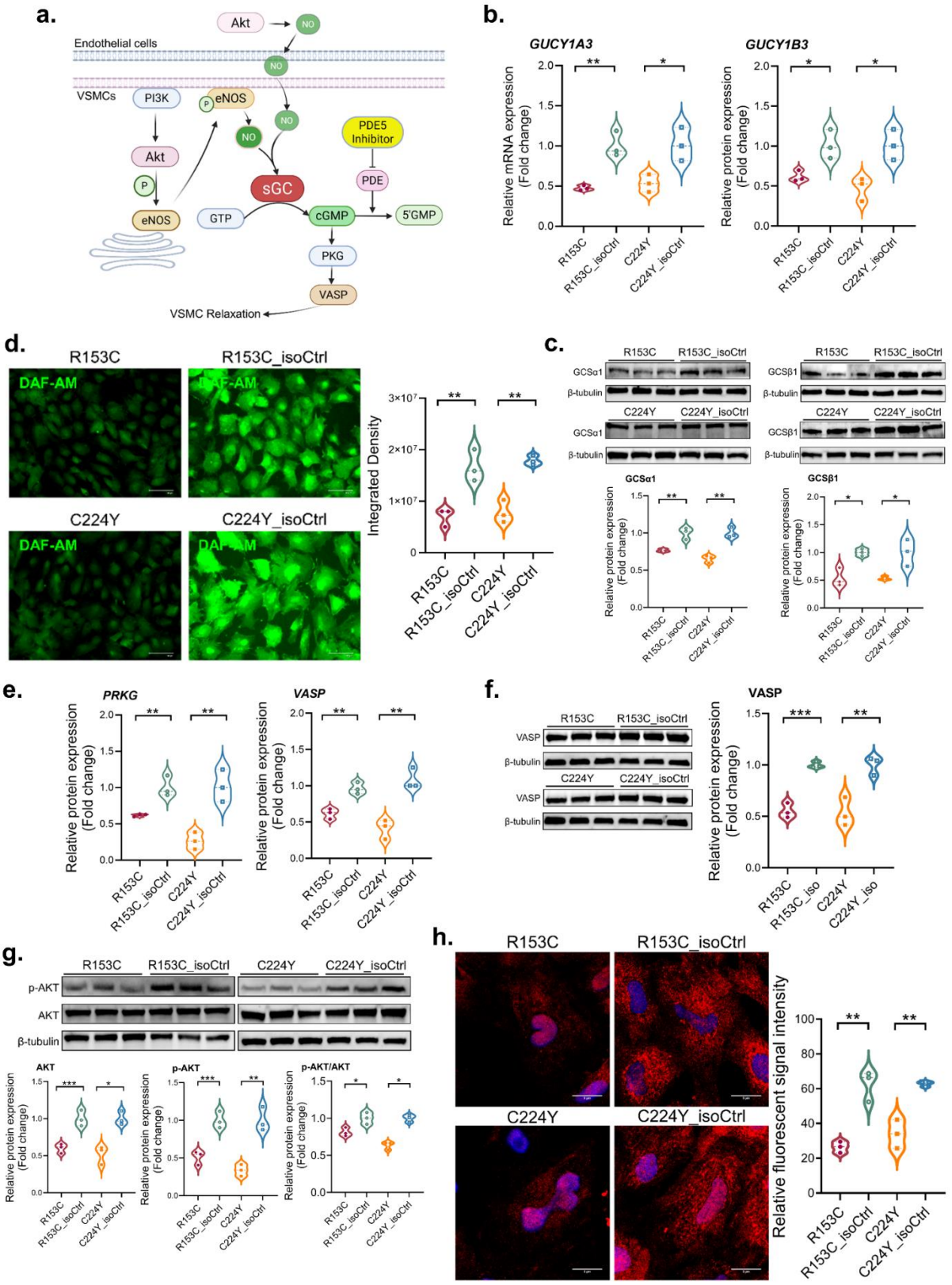
a.
Endothelial cells
VSMCs
Akt
NO
PI3K
eNOS
P
sGC
GTP
cGMP
5'GMP
PDE5 Inhibitor
PDE
PKG
VASP
VSMC Relaxation
b.
GUCY1A3
GUCY1B3
Relative mRNA expression (Fold change)
Relative protein expression (Fold change)
R153C
R153C_isoCtrl
C224Y
C224Y_isoCtrl
d.
DAF-AM
Integrated Density
c.
GCSα1
GCSβ1
β-tubulin
e.
PRKG
VASP
f.
VASP
β-tubulin
g.
p-AKT
AKT
β-tubulin
p-AKT/AKT
h.
Relative fluorescent signal intensity

**Figure 8.**

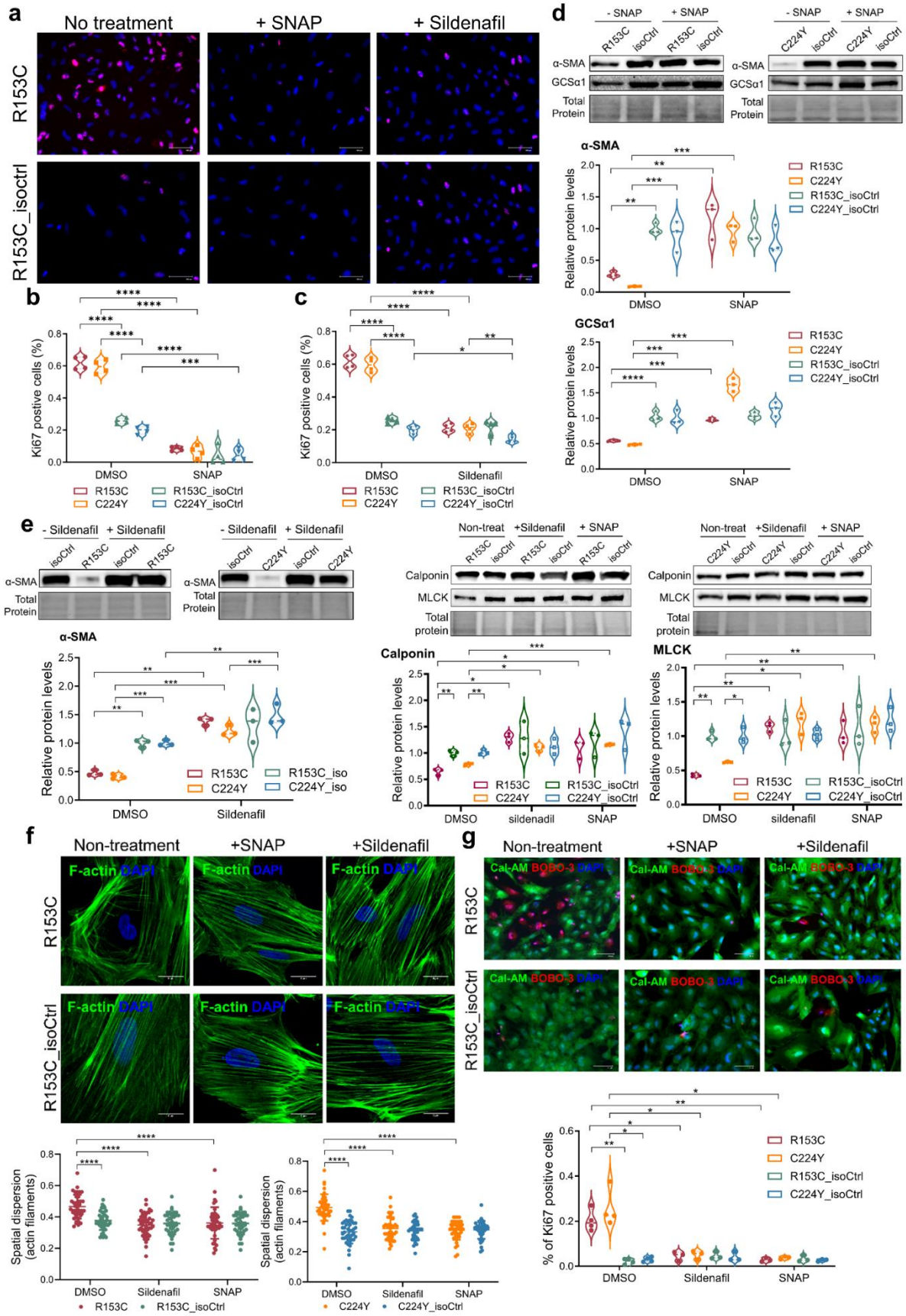
a
No treatment
+ SNAP
+ Sildenafil
R153C
R153C_isoctrl
b
Ki67 postive cells (%)
DMSO
SNAP
R153C
C224Y
R153C_isoCtrl
C224Y_isoCtrl
c
Ki67 positive cells (%)
DMSO
Sildenafil
d
- SNAP
+ SNAP
R153C
isoCtrl
C224Y
α-SMA
GCSα1
Total Protein
Relative protein levels
e
- Sildenafil
+ Sildenafil
Non-treat
+Sildenafil
Calponin
MLCK
Total protein
R153C_iso
C224Y_iso
sildenadil
sildenafil
f
Non-treatment
+SNAP
+Sildenafil
F-actin DAPI
Spatial dispersion (actin filaments)
g
Cal-AM BOBO-3 DAPI
% of Ki67 positive cells

**Figure 9.**

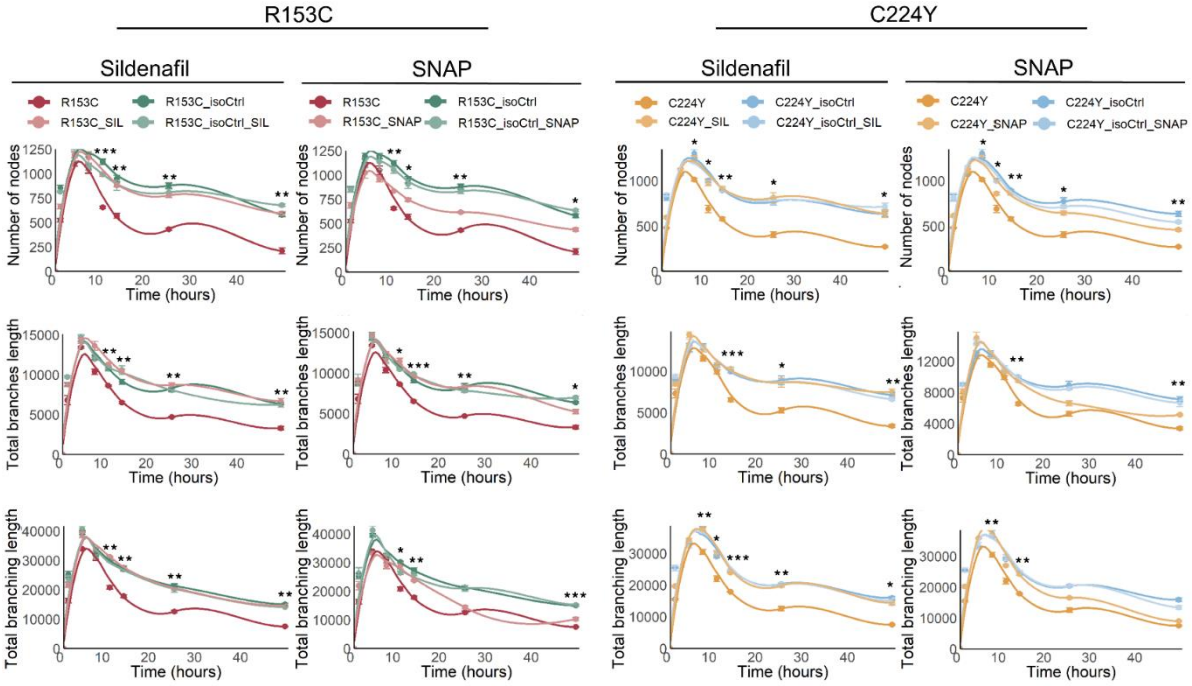
R153C
C224Y
Sildenafil
SNAP
Sildenafil
SNAP
R153C
R153C_isoCtrl
R153C_SIL
R153C_isoCtrl_SIL
R153C
R153C_isoCtrl
R153C_SNAP
R153C_isoCtrl_SNAP
C224Y
C224Y_isoCtrl
C224Y_SIL
C224Y_isoCtrl_SIL
C224Y
C224Y_isoCtrl
C224Y_SNAP
C224Y_isoCtrl_SNAP
Number of nodes
Total branches length
Total branching length
Time (hours)